

1 Large Scale atmospheric forcing and topographic 2 modification of precipitation rates over High Asia

3 —

4 A neural network based approach 5

6 Lars Gerlitz, Olaf Conrad & Jürgen Böhner

7 University of Hamburg, Institute of Geography, Bundesstraße 55, 20146 Hamburg,
8 Germany

9 correspondence to: L. Gerlitz (lars.gerlitz@uni-hamburg.de, Tel: 0049-40-42838-
10 4956)

12 13 **Abstract**

14
15 The heterogeneity of precipitation rates in high mountain regions is not sufficiently captured
16 by state of the art climate reanalysis products due to their limited spatial resolution. Thus
17 there exists a large gap between the available data sets and the demands of climate impact
18 studies. The presented approach aims to generate spatially high resolution precipitation fields
19 for a target area in Central Asia, covering the Tibetan Plateau, the adjacent mountain ranges
20 and lowlands. Based on the assumption, that observed local scale precipitation amounts are
21 triggered by varying large scale atmospheric situations and modified by local scale
22 topographic characteristics, the statistical downscaling approach estimates local scale
23 precipitation rates as a function of large scale atmospheric conditions, derived from the ERA-
24 Interim reanalysis, and high resolution terrain parameters. Since the relationships of the
25 predictor variables with local scale observations are rather unknown and highly non-linear, an
26 Artificial Neural Network (ANN) was utilized for the development of adequate transfer
27 functions. Different ANN-architectures were evaluated with regard to their predictive
28 performance.

29 The final downscaling model was used for the cellwise estimation of monthly precipitation
30 sums, the number of rainy days and the maximum daily precipitation amount with a spatial
31 resolution of 1 km². The model was found to sufficiently capture the temporal and spatial
32 variations of precipitation rates in the highly structured target area and allows a detailed
33 analysis of the precipitation distribution. A concluding sensitivity analysis of the ANN model
34 reveals the effect of the atmospheric and topographic predictor variables on the precipitation
35 estimations in the climatically diverse subregions.

1 Introduction

2

3 The large scale spatial pattern and the seasonal and interannual variability of precipitation
4 rates over Central and High Asia has been widely studied, particularly with regard to its
5 impact on downstream hydrological regimes and hence on the climate-sensitive agriculture
6 dominated economies of the highly populated downstream areas (Akhtar et al., 2008; Mall et
7 al., 2006; Matthews et al., 1997). The main rivers of South and East Asia such as Indus,
8 Ganges, Brahmaputra, Huang-He and Yangtze have their upper catchment areas on the
9 Tibetan Plateau or in the adjacent mountain regions and are mainly fed by the enhanced
10 precipitation rates compared with the surrounding lowlands and by snow melting in spring.
11 Glacial runoff contributes to a lesser extent but is crucial for the base flow during dry season
12 (Immerzeel and Bierkens, 2010). The glacial dynamics are likewise distinctly influenced by
13 the local- and mesoscale climate variability (Maussion et al., 2014). Particularly for the
14 investigation of the climatic influence on the fragile ecosystems of Central and High Asia
15 spatial high resolution climate data are required. While the temporal and spatial variations of
16 near surface temperatures over Central and High Asia have been modeled with reliable results
17 (Böhner, 2006; Gerlitz et al., 2014), the accuracy and spatial resolution of available gridded
18 precipitation estimates do not satisfy the demands of climate impact studies so far (Schoof,
19 2013). Gridded climate reanalysis products, such as ERA-Interim, adequately simulate the
20 large scale atmospheric features over Asia, but fail to capture the topographic variability of
21 precipitation rates over the highly structured target area. Often reanalysis products are refined
22 by means of dynamical downscaling applications, which employ Regional Climate Models
23 (Maussion et al., 2014). However, due to exponentially increasing computational demands
24 with rising spatial resolution, most studies focus on very limited target domains or time
25 frames. Dynamically downscaled fields for larger regions seldom achieve resolutions below
26 10 km and thus still do not address typical boundary layer processes on the meteorological
27 micro β to meso γ scale, such as topographically induced convective systems or local scale
28 orographic precipitation. In contrast, less computer demanding statistical downscaling
29 approaches aim to develop empirical transfer functions, linking independent large scale
30 atmospheric parameters to near surface observations, in order to predict local scale climate
31 conditions under altering synoptic situations. Since statistical downscaling applications are
32 usually calibrated based on point scale observations, they enable the estimation of near
33 surface climates for specific locations. Although some studies indicate, that the preciseness of
34 statistical downscaling applications is comparable with dynamical downscaling approaches

1 (Schoof, 2013), the generation of fully distributed climatic fields by means of statistical
2 techniques remains challenging so far (Maraun et al., 2010). Against this background, we
3 present a novel empirical approach, which enables an estimation of spatially high resolution
4 monthly precipitation fields, basically merging statistical downscaling of large scale
5 atmospheric fields and DEM-based terrain parameterization methods. Therefore we consider
6 local scale precipitation as a function of large scale atmospheric parameters on the one hand
7 and a local scale terrain induced modification on the other. Selected terrain parameters were
8 developed and evaluated with regard to their representation of local scale atmospheric
9 processes, which typically lead to precipitation occurrence. Subsequently statistical
10 relationships between large scale atmospheric conditions, terrain parameters and local scale
11 precipitation observations were analyzed and adequate transfer functions were developed.
12 Based on the assumption, that the atmosphere-topography interactions are highly nonlinear,
13 we utilized an artificial neural network (ANN) approach for the analysis of the statistical
14 relationships. Neural networks stand out due to their ability to approximate any continuous
15 multidimensional function and their capability to handle the interactions of interconnected
16 predictors. Particularly for the examination of complex systems with unknown relationships
17 between several predictor and predictant variables, neural networks have been increasingly
18 used in the field of climate- and geoscience.

19 Due to the integration of physically based terrain parameters for the estimation of local scale
20 precipitation rates, the presented approach remains physically consistent and can be utilized
21 for the development of local scale climate change scenarios. All methods have been applied
22 on a 64-bit windows personal computer , which reflects the low computational demands of the
23 approach and its suitability for climate and climate impact studies in environmental offices
24 and research units, even in Central Asian countries

25 In the following section, we firstly provide a brief overview of large scale circulation modes,
26 associated pluviometric regimes and their topographic modifications over the target area.
27 Subsequently, we introduce the utilized large scale atmospheric data sets and the derivation of
28 precipitation-relevant terrain parameters in section 3.1. Section 3.2 addresses the
29 implementation and validation of the statistical model. Subsequently, the spatio-temporal
30 variability of precipitation rates over the target area as well as the influence of the major
31 atmospheric and topographic predictors is analyzed in section 3.

32
33
34

2 Large scale circulation modes, pluviometric regimes and the role of topography

The target area, shown in Fig. 1, covers the Tibetan Plateau and the main mountain ranges of High Asia, such as the Himalayan Arc, the Kunlun Shan and the Quilian Shan. The adjacent Indus-Ganges Lowlands, the Tarim Basin and the Red Basin define the borders of our target domain. Extending from 80° to 105° E and 25° to 42° N, the pluviometric regimes of this vast area are controlled by both, tropical-subtropical as well as extratropical circulation systems. Seasonal shifts in large-scale circulation modes and the associated alternation of air masses lead to a distinct hygric seasonality commonly subsumed under the term ‘monsoon’. Although this characteristic differentiation between a rather moist summer and a dry winter season is valid for most of the target area, precipitation regimes and its spatial domains differ in terms of air masses and involved synoptic processes. In general, the target area is controlled by three major pluviometric regimes: the East Asian summer monsoon, the South Asian summer monsoon (syn. Indian summer monsoon) and the extratropical westerlies and its associated fronts and disturbances (Böhner, 2006; Maussion et al., 2014).

[Fig. 1]

In summer the continental areas of the target area and especially the elevated Tibetan Plateau act as a heat source, which triggers the development of the autochthonous ‘plateau monsoon’, a shallow direct circulation mode converging above the Tibetan Plateau (Flohn, 1987). Enhanced flux of sensible heat from the elevated heat source and the release of latent heat in high reaching convection clusters over the north-eastern Indian plains and adjacent mountain ranges lead to the formation of a warm anticyclone in the mid to upper troposphere (monsoon high) and establishes the 500–200 hPa layer over southern Tibet as the earth’s free-atmosphere warm pole. The resulting reversal of upper-troposphere temperature gradients in the Indian-Indonesian sector forces the development of the Tropical Easterly Jet, a permanent component of the large-scale summer monsoon system, which controls trajectories of monsoonal disturbances south of the Himalayas tracking from east to west as well as the alternating formation of convection cells and frontal rains in south-eastern Tibet (Böhner, 2006; Domrös, 1988; Flohn, 1987). Due to lower radiation income and thermal capacity, strong high pressure cells form over the adjacent Indian and Pacific Ocean. Thus the shallow trough over Tibet leads to converging moist air masses over the Asian continent (Maussion et

1 al., 2014). The Himalayan Arc acts as a barrier to the near surface monsoonal currents, which
2 results in an orographic uplift of moist air masses and strong convection over India and the
3 Southern slopes of the Himalayas so as to the formation of the monsoon trough over the
4 Indian Lowlands (Böhner, 2006). The main moisture fluxes for the South Asian summer
5 monsoon originate over the Bay of Bengal and lead to intensive and perpetual precipitation
6 over the eastern Indus-Ganges Lowlands and the adjacent mountain ranges. The moist air
7 masses penetrate the meridional Three River Gorges and lead to enhanced precipitation rates
8 in South Eastern Tibet. A minor monsoonal current advects moist air masses from the Arabian
9 Sea into Western India and the Western Himalayas (Sigdel and Ikeda, 2012). Since the
10 western monsoonal current is weaker, a clear east-west gradient of summer precipitation rates
11 over the Indus-Ganges Lowlands and the Himalayan Arc can be observed (Böhner, 2006;
12 Wulf et al., 2010). The Central and Western Tibetan Plateau is less directly influenced by
13 monsoonal air masses. Precipitation events are mainly associated with diurnal local scale
14 convection due to high rates of solar irradiation (Maussion et al., 2014).

15 The easternmost parts of the investigation area are mainly influenced by the East Asian
16 summer monsoon. The advection of dry continental air from northern directions and the flux
17 of moist tropical air originating from the western Pacific lead to intensive front formation in
18 the middle troposphere of the polar mixing zone. The resulting quasi-stationary fronts and its
19 associated rain regimes cover large domains over East Asia (Böhner, 2006).

20 The northern part of the target area remains north of the ITCZ during summer season and
21 hence is mainly influenced by extratropical westerlies. However due to the shadowing effect
22 of the Pamir, Karakoram and Tian Shan mountain ranges (outside of the target area) the Tarim
23 Basin remains dry with summer precipitation rates below 25mm (Xu et al., 2004). Only the
24 elevated and western exposed regions of the Kunlun and Quilian Shan receive summer
25 precipitation due to western cyclonic activity (Böhner, 2006). During post monsoon season
26 the pressure cells over Asia and the adjacent oceans dissolve and the ITCZ shifts southward.
27 The area influenced by western circulation patterns spreads south and reaches the Himalayan
28 Arc in winter season. The Tibetan Plateau and the continental regions of Central Asia now act
29 as a cold source, resulting in the formation of the Asiatic High over Mongolia and northern
30 China. The associated strong pressure gradients between the high pressure cell over Asia and
31 its counterparts, the Aleutian Low over the Pacific Ocean and the ITCZ over the Indian
32 Ocean, lead to a divergent near surface flow over Central and High Asia. Thus the target area
33 is under influence of dry continental air masses. The 200 hPa jetstream at the planetary frontal
34 zone reaches its southernmost position in January at 35 °N. Due to the blocking effect of the

1 Tibetan Plateau the jetstream is divided into two branches. While the northern current is
2 situated near the Altai Mountains (north of the target area), the southern branch follows the
3 slopes of the Himalayas. The western Himalayas, particularly west facing slopes, receive a
4 considerable amount of winter precipitation associated with the uplift of the westerly flow and
5 western disturbances brought by the 200 hPa jetstream. Thus winter precipitation events in the
6 target area are mainly triggered by circulation modes of the temperate latitudes (Böhner,
7 2006; Filippi et al., 2014; Maussion et al., 2014; Wulf et al., 2010). The eastern parts of the
8 study area receive less precipitation due to the shadowing effect of the Tibetan Plateau and the
9 mountain ranges of High Asia. The Indian plains are under the influence of the subtropical
10 subsiding motion of the Hadley cell and are characterized by stable atmospheric conditions
11 (Böhner, 2006). In spring the pressure gradients over Asia decrease due to increasing solar
12 irradiation. The northern branch of the 200 hPa jetstream strengthens, the major trajectories of
13 the western disturbances shift northward. The Indus-Ganges Lowlands and especially the
14 southern Himalayan slopes receive high solar radiation, which results in occasional
15 convective precipitation events (Romatschke et al., 2010).

16 The investigation of the interannual variability of precipitation rates over Central and High
17 Asia often focuses on the summer monsoon season. Most studies (Li and Yanai, 1996; Peings
18 and Douville, 2010; Prodhomme et al., 2014) reveal that the intensity of the monsoon highly
19 depends on the magnitude of pressure gradients. Since the formation and intensity of the low
20 pressure cell over Asia is mainly triggered by the radiative heating of the Tibetan Plateau, an
21 enhanced snow cover during winter and spring increases the surface albedo and results in a
22 delayed and reduced formation of the thermal low and subsequently in decreasing summer
23 precipitation amounts. Moreover, many studies highlight the importance of the Southern
24 Oscillation for the intensity of monsoonal precipitation (Sankar et al., 2011; Shrestha, 2000),
25 although some studies illustrate, that the correlation of the SOI-Index and the Indian and the
26 East-Asian summer monsoon precipitation weakened during recent decades (Kumar et al.,
27 1999; Wang and He, 2012). Studies by Pokhrel et al. (2012) and Sigdel and Ikeda (2012)
28 indicate that El Nino events are accompanied by reduced moisture fluxes into South Asia.
29 Preethi et al. (2011) point out, that the severe 2009 drought over India was at least partially
30 triggered by a weak El Nino event. The variability of winter precipitation is mainly related to
31 the magnitude of the pressure gradients and the position of the planetary frontal zone and the
32 accompanying westerly jetstream (Dimri et al., 2013).

33 On the local scale the precipitation distribution over the target area is extremely modified due
34 to the various interactions of moist air masses with complex topography and the

1 accompanying local scale atmospheric processes (Chen et al., 2014; Guan et al., 2009; Suprit
2 and Shankar, 2008). Many studies show, that the elevation plays a crucial role for the
3 precipitation distribution, although the vertical precipitation gradient in high mountain regions
4 varies considerably in different target areas. While some studies indicate increasing
5 precipitation amounts up to highest elevations, others assume an elevational threshold,
6 followed by stationary or even decreasing values (Barry, 2012). The near surface monsoonal
7 currents during summer season generate high precipitation rates up to elevations of 4000 m,
8 followed by a sharp decrease above at the southern Himalayan slopes (Barros et al., 2000;
9 Shrestha et al., 2012). The cyclogenetic winter precipitation reaches higher elevations, due to
10 orographic uplift of the westerly flow. In general the windward slopes receive enhanced
11 precipitation. The orographic precipitation reaches annual amounts of up to 10.000 mm/a in
12 the Kashi Hills in Northern India. In contrast, the leeward areas of the Trans-Himalaya are
13 characterized by arid conditions even during summer season (Böhner, 2006). Based on the
14 remote sensing derived Tropical Rainfall Measuring Mission (TRMM) Bookhagen and
15 Burbank (2006) show, that the topography of the Southern Himalayan slopes is the main
16 trigger for the local scale precipitation distribution. While the central Himalayas are
17 characterized by a so called one-step-topography, which results in a distinct band of maximal
18 precipitation rates south of the main mountain ranges, the eastern and western parts show a
19 second band of high precipitation at lower elevations due to the orographic barrier of the
20 lesser Himalayas. (Böhner, 2006; Maussion et al., 2014). The precipitation rates in high
21 mountain regions are further modified by autochthonous local scale circulations, such as the
22 diurnal valley-mountain breeze. The enhanced irradiation at the mountain slopes leads to
23 slope-upward winds and subsiding air motions over the valley bottoms. This results in
24 convection and occasional precipitation events over the slopes, while the valleys remain dry
25 (Böhner and Antonić, 2009).

26

27 **3 Data and Methods**

28

29 Gridded climate reanalysis products, such as ERA-Interim (developed at the European Center
30 for Medium Range Weather Forecast, ECMWF), simulate 6-hourly large scale atmospheric
31 fields for 60 pressure levels between 1000 and 1 hPa over Asia with a horizontal resolution of
32 0.7° lat/long (T255) (Berrisford et al., 2009; Dee et al., 2011). Since the ERA-Interim
33 reanalysis combines modeling results with ground and radiosonde observations and remote

1 sensing data using a data assimilation system the free atmospheric fields can be considered as
2 the best guess of the current large scale atmospheric situation for every time step. Many
3 studies reveal that ERA-Interim adequately captures the variability of relevant free air
4 meteorological parameters, even over complex mountain regions (Bao and Zhang, 2012; Gao
5 et al., 2012). Recent evaluations of different reanalysis products show that ERA-Interim has
6 the best accordance with in situ observations derived from near surface meteorological
7 records (Bao and Zhang, 2012) and radiosonde observations over the Tibetan Plateau (Wang
8 and Zeng, 2012) and the Central Himalayan Arc (Jin-Huan et al., 2013). These results were
9 particularly evident for temperature, wind direction and velocity and hydroclimatological
10 parameters. Due to the assimilation of in situ radionsonde and near surface observations we
11 assume that the precipitation relevant moisture fluxes are well represented by ERA-Interim.
12 Sigdel and Ikeda (2012) show that the interannual variability of moisture transports into the
13 target area (e.g. because of variations of the Southern Oscillation) can be captured by
14 reanalysis products. However, their coarse resolution is insufficient to represent the spatial
15 variability of sub-grid atmospheric processes in the highly structured study area. For the
16 analysis of local scale precipitation rates we utilized daily observations from 173
17 meteorological stations which were available from 1989 onwards. 157 records were used for
18 the model calibration based on the period from 1989 to 2000. Further 16 station records for
19 the period from 2000 to 2011 were used for the evaluation of the modeling approach (Fig. 1).
20 Thus the validation data set is spatially and temporally independent from the model
21 implementation. The station records for the evaluation procedure were subjectively chosen
22 with the objective to represent all major geographic subregions of the target area and their
23 specific climate characteristics. The data sets in general showed a sound data quality, missing
24 values were deleted. The observations for China and Tibet were provided by the China
25 Meteorological Administration, the records for Nepal were supplied by the Department of
26 Hydrology and Meteorology, Kathmandu / Nepal. All station records were quality proofed
27 using the Neumann-ratio for annual precipitation sums. Further the cumulative residuals were
28 tested as suggested by Buishand (1982). Records showing significant inhomogeneities on the
29 99 % level were rejected. The precipitation time series were aggregated to monthly sums. For
30 a rough assessment of the temporal precipitation distribution we used the maximum daily
31 amount as well as the number of rainy days as additional predictant variables.

32
33

3.1 Atmospheric and topographic predictors

For the characterization of the large scale atmospheric pressure distribution over Asia a principle component analysis (PCA) of the ERA-Interim 500 hPa geopotential height (GPH) fields was conducted for the macrogeographical region between 50°N and 10°S and 30°E and 140°E. This allows the identification of the major spatial modes and the temporal variability of the atmospheric circulation over the target area. The PCA-analysis decomposes the time series of gridded GPH fields to a small number of orthogonal atmospheric patterns (referred to as eigenvectors or Empirical Orthogonal Functions, EOFs) and accompanying uncorrelated time indices (scores) (Hannachi et al., 2006). The atmospheric pattern for every time step can then be described as a linear combination of the EOFs and scores. Typically the major part of the large scale atmospheric variability can be explained by only a small number of EOF-fields (Hannachi et al., 2007). This leads to a reduction of the dimensionality of complex systems and removes internal redundancies. The PCA was conducted based on anomalies of the 500 hPa ERA-Interim monthly mean GPH compared with the longtime mean for the period from 1989 to 2010. For the computation we utilized the package prcomp within the Free and Open Source Software R. We considered those fields which contribute to more the 1% of the total variance of the spatio-temporal GPH distribution. Since the position of the major pressure cells over Asia and the adjacent oceans determines the prevailing wind directions and the moisture transport into the target area, the EOF-fields are useful to interpret the circulation variability and the accompanied precipitation forming atmospheric processes. The scores indicate the relevance of the EOF patterns for the pressure distribution of each month and were used as large scale predictors for the presented downscaling approach.

Fig. 2 shows the major six EOF-fields and the appendent time series of scores, as well as their portion of variance explained. The first EOF indicates the seasonal shift of the ITCZ and the associated north-southern pressure gradient between the Asian continent and the Indian Ocean. During summer the continent is characterized by a thermal low pressure cell, which results in an uplift of the 500 hPa GPH. At the same time the Indian Ocean is under influence of the Southern branch of the Hadley cell, which results in higher sea level pressure and a decrease of the 500 hPa level GPH. In winter season the large scale atmospheric conditions turn due to the southward shift of the ITCZ. The scores of the first EOF show a clear annual cycle, the summer circulation pattern is characterized by positive, the winter pattern by negative scores. The second EOF field addresses a pressure gradient from east to west over the Asian continent. Again the scores suggest an annual cycle of the second EOF, with mainly

1 positive values during summer and negative values during winter season. This is attributed to
2 the formation of a thermal low pressure cell over Central Asia during summer. However the
3 time series of scores show an interannual variability, which is significantly correlated with the
4 index of the Southern Oscillation, defined as $SOI = \frac{\Delta P - \Delta P_{avg}}{s_{\Delta P}}$, where ΔP indicates the sea
5 level pressure difference between Tahiti and Darwin. ΔP_{avg} is the mean pressure difference
6 and $s_{\Delta P}$ is the accompanying standard deviation ($r=-0.51$, $p=0.99$). Particularly the extreme
7 1997/1998 El-Nino event is clearly evident in the time series of EOF-scores. (Kirono et al.,
8 1999; Slingo and Annamalai, 2000; Wang et al., 2002). The first two EOFs already contribute
9 to 84.1% of the temporal large scale variability of the GPH over the selected region. The third
10 EOF-field (which explains additional 4.4 % of the GPH variability) indicates the uplift and
11 lowering of the 500 hPa level over Northern India and South East Asia.

12

13 [Fig. 2]

14

15 This band coincidences with the position of the Tropical Easterly Jet during summer season
16 and the trajectories of tropical disturbances (Parth Sarthi et al., 2014).

17 The fourth EOF pattern addresses an east-west oriented pressure gradient over the Indian
18 Ocean. Pattern five alludes to variations of the 500 hPa level GPH over the Southern Indian
19 Ocean, pattern six indicates variations of the simultaneous formation of pressure cells over the
20 Arabian Sea and the Australian continent.

21 For the characterization of precipitation relevant synoptic situations we further processed the
22 ERA-Interim monthly means of relative humidity at the 500 and 200 hPa level. These fields
23 were resampled to a grid size 1 km² using thin plate spline and were extracted for every single
24 meteorological station. Since the downscaling approach utilizes only free atmospheric fields
25 as large scale predictor variables, the interpolation to high spatial resolution appears
26 reasonable. Many studies (Corbosiero and Molinari, 2002; Frank and Ritchie, 2001; Wingo
27 and Cecil, 2009) mention the vertical wind shear between the 500 and 200 hPa level as an
28 important factor for the spatial and temporal precipitation distribution, particularly with
29 regard to tropical disturbances. Thus the wind shear was derived from the ERA-Interim
30 reanalysis and likewise resampled to the required resolution of 1 km².

31 For the analysis of interactions between the large scale synoptic situation and the varying
32 topographic settings of the target area, specific terrain parameters were integrated into the
33 downscaling approach. These were derived from the SRTM digital elevation model (Farr et

1 al., 2007) and aggregated to a 1 km² resolution. Primary the raw surface elevation (Z) controls
 2 the precipitation distribution in complex terrain (Daly et al., 1994). The vertical precipitation
 3 gradient in mountainous regions is often exaggerated due to the diurnal mountain-valley
 4 circulation and the associated convection at the mountain slopes. To account for the spatial
 5 variations of terrain induced convection, we utilized the relative elevation above the channel
 6 network (Z_{rel}) as an additional predictor variable. Therefore the channel lines were identified
 7 and interpolated for the target domain. The elevation above channel line is subsequently
 8 calculated as a difference of the surface elevation and the interpolated channel altitudes. The
 9 methods for the derivation of the relative elevation above the channel network are available as
 10 a complete tool in the Free and Open Source Geographical Information System SAGA
 11 (Böhner and Antonić, 2009).

12 Orographic precipitation, resulting from the uplift of moisture-bearing air masses at windward
 13 slopes of topographic barriers and the related leeward rain shadow, is probably the most
 14 prominent feature of the spatial precipitation distribution in the target area. Based on the
 15 assumption, that the windward impact on the precipitation intensity depends on the prevailing
 16 large scale wind direction and on the elevation of the orographic barrier, a wind-index (as
 17 suggested by Böhner and Antonić (2009)) was used for the presented study. For the Tibetan
 18 Plateau with its mean elevation between 4000 and 5000m, the 500 hPa wind field can be
 19 considered as near surface, but also the wind and leeward effects of the major mountain
 20 ranges influence the 500 hPa level wind field. It should be mentioned, that the 500 hPa level
 21 does not represent near surface conditions for the peripheral lowlands, however we assume
 22 that the annual cycle of prevailing wind directions is depicted by the 500 hPa level. Thus we
 23 resampled the monthly mean ERA-Interim 500 hPa wind fields to the target resolution of 1
 24 km² and subsequently derived the wind- and leeward positions. For every grid cell the wind
 25 trajectories were followed and the weighted vertical angles of the flow currents were analyzed
 26 using the following equations.

27 The windward index H_W and the leeward index H_L were calculated to:

28

$$29 \quad H_W = \frac{\sum_{i=1}^n \frac{1}{d_{WHi}} * \tan^{-1}\left(\frac{d_{WZi}}{d_{WHi}}\right)}{\sum_{i=1}^n \frac{1}{d_{LHi}}} + \frac{\sum_{i=1}^n \frac{1}{d_{LHi}} * \tan^{-1}\left(\frac{d_{LZi}}{d_{LHi}}\right)}{\sum_{i=1}^n \frac{1}{d_{LHi}}} \quad (1)$$

30

$$31 \quad H_L = \frac{\sum_{i=1}^n \frac{1}{\ln(d_{WHi})} * \tan^{-1}\left(\frac{d_{LZi}}{d_{WHi}}\right)}{\sum_{i=1}^n \frac{1}{\ln(d_{LHi})}} \quad (2)$$

32

1 were d_{WHi} and d_{LHi} refer to the horizontal distances in windward and lee direction and d_{WZi}
2 and d_{LZi} are the corresponding vertical distances compared with the considered raster cell.
3 The second summand in formula (1) accounts for the leeward impact of previously traversed
4 mountain chains. The logarithmized horizontal distances in formula (2) lead to a longer
5 distance impact of leeward rain shadow. The final wind effect parameter, which is supposed to
6 be related with the interaction of the large scale wind field and the local scale precipitation
7 characteristics, is calculated to $H = H_L * H_W$ and takes values between 0.7 for leeward and
8 1.3 for windward positions (Böhner and AntoniĆ, 2009). The cellwise calculation of the wind
9 effect is likewise fully implemented in SAGA-GIS.

10
11 [Fig. 3]

12
13 Fig. 3 shows the spatial distribution of the wind effect as well as the mean 500 hPa wind field
14 exemplarily for January and July 2010. The upper picture shows the complete target area, the
15 lower one is an enlargement of the Central Himalayan Arc. The winter situation is
16 characterized by a homogenous westerly flow which results in high values of the wind effect
17 parameter at the western slopes, particularly at the margins of the Kunlun Shan, Quilian Shan
18 and the Himalayas. During summer the thermal low over the Tibetan Plateau is fully
19 established, resulting in a converging flow pattern at the 500 hPa level. The north-westerly
20 monsoonal currents over Southern Asia lead to maximal values of the wind effect parameter
21 at the southern Himalayan slopes. Especially the first mountain ranges north of the Nepalese
22 border and the major Himalayan peaks are characterized by strong windward positions. In
23 contrast the east-west oriented valleys of Central Nepal are located in the rain shadow of the
24 lower Himalayas. The strong leeward position of the Trans-Himalayan valleys north of the
25 major peaks is particularly well captured by the spatial distribution of the wind effect
26 parameter.

27 To account for varying interactions of large scale atmospheric processes and topographic
28 characteristics in the versatile subregions of the target area the geographical coordinates (lat. /
29 long.) were considered as further explanatory variables for the presented downscaling
30 approach.

31 Finally all predictor and predictant variables were normalized by subtracting the mean values
32 and dividing by the corresponding standard deviation.

3.2 Implementation and Evaluation of an ANN-Model

Traditional statistical methods, most notably linear models, have been frequently used for the quantification of statistical relationships and the implementation of transfer functions (e.g. Böhner, 2006) although the actual predictor-predictant relations are often highly non-linear (Gerlitz, 2014; Sauter and Venema, 2011). Further the data sets used often violate the statistical conditions, e.g. in case of intercorrelated predictor variables or non-normal-distributed and non-homogenous residuals (Schönwiese et al., 2010; Schoof and Pryor, 2001). During the last decade complex machine learning algorithms such as Artificial Neural Networks became more prominent in the field of geoscientific research and have been utilized e.g. for hydrological simulations (Dawson and Wilby, 2001; Jain and Kumar, 2007), snow cover prediction (Sauter and Venema, 2011) and habitat modeling (Özesmi and Özesmi, 1999), but also for statistical downscaling and climate modeling applications. For the analysis and prediction of the variability and change of monsoonal precipitation rates over India various recent studies applied ANNs with reliable results (Chattopadhyay, 2007; Shukla et al., 2011; Singh and Borah, 2013). In the field of precipitation downscaling ANNs were utilized (amongst others) by Coulibaly et al., (2005), Dibike and Coulibaly (2006), Mekanik et al. (2013) and Tomassetti et al. (2009). All studies highlight the complexity and non-linearity of the climate system with particular regard to precipitation-forming processes. A comprehensive review of studies on rainfall prediction based on neural network applications is given by Ranjan Nayak et al. (2013). Schoof and Pryor (2001) compared the predictive performances of neural network based downscaling approaches with linear regression based methods and concluded that ANNs superiorly capture complex interactions between the large scale synoptic patterns and local scale observations, although they point out, that the results of precipitation downscaling approaches do not achieve the quality of comparable temperature estimations.

Compared to linear models, ANNs stand out due to their flexibility and their capability to approximate any non-linear continuous function. The data driven non-parametric approach can identify input-output relationships without any prior assumptions and can handle intercorrelated predictor variables, which is advantageous if complex systems are to be analyzed and the specific type of internal relationships and interactions is unknown (Günther and Fritsch, 2010; Sauter et al., 2009). Inspired by our conception of the human brain, ANNs are composed of numerous simple parallel operating processing units (referred to as neurons)

1 and associated weights (synapses). The neurons are generally arranged in layers, starting with
 2 the input layer, which contains one neuron for each independent variable X_i , one or more
 3 hidden layers with an arbitrary number of neurons for the processing of the data and one
 4 output layer, which releases the final modeling results. Since an ANN with one hidden layer
 5 can already approximate any continuous differentiable function (Schoof and Pryor, 2001)
 6 multilayer ANNs are seldom used for regression applications.

7
 8 [Fig. 4]

9
 10 Fig. 4 shows an exemplarily neural network architecture with three input variables, one
 11 hidden layer with two processing units and one output variable. The input passes the vector of
 12 time series of the independent variables to the hidden neurons. These receive a signal, which
 13 is determined by the so called integration function net_j , defined as a weighted linear
 14 combination of the predictant vectors. To account for non-linearities of the input-output
 15 relationships the neurons process the signal by means of the activation function φ , which is
 16 usually defined as a sigmoid logistic function, mapping the values of the integration function
 17 to a domain $\in [0;1]$. The value 1 refers to a strong effect of the particular linear combination
 18 of the input vectors for the output result, while 0 indicates a negligible influence. In the final
 19 output layer the activation function is linear. For the calculation of the output o_j of any neuron
 20 j , the activation function is applied to the net result of the weighted linear combination net_j .

21
 22
$$o_j = \varphi (net_j) \quad with \quad net_j = \sum_{i=1}^n w_i * x_i \quad and \quad \varphi = \frac{1}{1+e^{-net_j}} \quad (3)$$

23
 24 Most ANNs are constructed using a three layer architecture with only one hidden layer, where
 25 the processing of the data is conducted. For the presented study we utilized a Feed-Forward
 26 ANN, i.e. the information flow is unidirectional. Each neuron receives signals from all nodes
 27 of the previous layer and passes the modified signal to the nodes of the subsequent one. The
 28 knowledge of an ANN is comprehended in the weights of the integration function. These are
 29 initially assigned as random values of the normal distribution. The initial network processes
 30 the input-vectors based on the integration and activation functions of the internal neurons and
 31 passes an output-signal to the final layer. Since the weights are randomly chosen, the output of
 32 the ANN model, compared with observed values, is primarily insufficient. Based on a
 33 learning sample the weights are subsequently iteratively adjusted with the aim of minimizing
 34 the error function, defined as the root mean square error of the desired predictant values and

1 the outcome of the ANN model. For the adjustment of weights several supervised learning
2 algorithms were developed, although most ANN applications are based on the so called
3 Backpropagation approach (Hecht-Nielsen, 1989). This algorithm calculates the gradient of
4 the error function with regard to modified weights backward in the network and shifts the
5 weights into the opposite direction of the partial derivatives based on a default learning rate.
6 The recursive application of the backpropagation procedure ensures the identification of a
7 local minimum of the error function and the corresponding weights. To discover the best
8 neural network for the regression of the local scale precipitation rates as a function of the
9 above mentioned predictor variables we utilized the resilient backpropagation approach,
10 which is fully implemented in the free and open source R-package neuralnet (Günther and
11 Fritsch, 2010). This algorithm increases the learning rate, if the direction of the error gradient
12 keeps its sign. If the sign turns, the learning rate is decreased automatically. This leads to an
13 accelerated convergence of the recursive adjustment of weights and avoids that a minimum is
14 missed due to a too large learning rate.

15 The most obvious degree of freedom of any ANN approach is its architecture, particularly the
16 number of neurons within the hidden layer. Although thumb rules for the best number of
17 neurons have been suggested (Basheer and Hajmeer, 2000), a general rule, defining the best
18 ANN architecture, could not be determined so far. While an ANN model with too many
19 neurons in the hidden layer tends to overfit, which results in a poor predictive performance, an
20 insufficient number of neurons leads to an over-generalization and hence a non-detection of
21 distinct non-linear relationships within the learning sample. The best ANN architecture highly
22 depends on the number of predictor and predictant variables, the number of cases and the type
23 and complexity of the statistical relationship (Sauter et al., 2009). Thus, for the identification
24 of an optimum ANN for the downscaling approach, we tested several ANN architectures with
25 regard to their predictive power. Starting with only one neuron in the hidden layer, the
26 complexity of the network was gradually increased. Due to exponentially increasing
27 computing demands of the learning phase, the maximum of neurons was set to 10. For every
28 number of neurons an ANN was implemented based on the learning sample containing
29 monthly time series of 157 meteorological stations for the period for 1989 to 2000. The
30 vectors of predictor variables were used as input nodes. As output variables the observed
31 monthly precipitation sum, the maximum of daily precipitation and the number of rainy days
32 were chosen. Every ANN realization was used to predict the output variables for an
33 independent evaluation data set. Due to the disproportionately high computing demands of
34 cross-validation techniques, we exemplarily evaluated the ANN performance based on time

1 series from 16 stations for the period 2001 to 2011 (see red dots in Fig. 1). These subjectively
2 chosen stations cover different climatic subregions and thus enable the evaluation of the
3 model under varying pluviometric regimes. The fact, that the evaluation data set is temporally
4 *and* spatially independent facilitates the prevention of overfitting of both, large scale
5 atmospheric and local scale topographic predictor variables. For the evaluation of the model,
6 the mean squared residuals of each station were calculated and normalized using the mean
7 and the standard deviation of the particular record of observations. This enables the
8 comparison of the model quality for stations with varying precipitation amounts. Fig. 5 shows
9 the mean squared error (in standard deviations) of the monthly precipitation sums for each of
10 the evaluation records. The ANN realizations with only a few neurons in the hidden layer
11 show large residuals for some stations. This is due to an extreme overestimation of
12 precipitation rates for the dry regions in the North of the study area (not shown). With
13 increasing complexity the model better captures the diverse climates of the target area and
14 improves the prediction performance for the evaluation data records. The ANN with 8 hidden
15 neurons was found to have the lowest prediction error of the monthly precipitation sums (with
16 values below 0.5 standard deviations for most of the meteorological stations) and hence was
17 used for the cellwise estimation of precipitation rates in the target area. The analysis of the
18 prediction power for the maximum daily precipitation and the number of rainy days revealed
19 similar results (not shown). For ANN architectures with more than eight hidden neurons the
20 prediction performance of the model decreased considerably. The maps in Fig 5 exemplarily
21 show the predicted fields of precipitation sums for the Central Himalayan region for July
22 2010 based on varying ANN architectures with N=1, N=8 and N=10 hidden neurons. The
23 simple ANN with only one neuron in the hidden layer does not capture the topographically
24 determined precipitation distribution and mainly depicts an elevational gradient of
25 precipitation sums with high values in the Indus-Ganges Lowlands and lower values in the
26 high mountains and on the elevated Tibetan Plateau. In contrast the ANN with 10 hidden
27 neurons clearly overfits the input-output relationships resulting in a rather unrealistic scattered
28 precipitation field, particularly over the highly complex terrain of the Southern Himalayan
29 slopes. The precipitation distribution predicted by the “best” ANN architecture with eight
30 hidden neurons depicts two major precipitation bands, one at the first topographic barrier of
31 the outer Himalayas and one at the southern margin of the highest mountain peaks as well as a
32 sharp decrease of precipitation amounts above 4000 m.

33 These results highly agree with previous studies on the topographically induced distribution
34 of precipitation rates in the target area (Bookhagen and Burbank, 2006; Maussion et al., 2014;

1 Shrestha et al., 2012) and support the reliability of the statistical model. Fig. 6 compares the
2 modeled and observed time series of monthly precipitation sums for the 16 independent
3 stations. The spatial distribution of precipitation (with annual precipitations sums ranging
4 from below 50 mm over the Tarim Basin to more than 2000 mm over the monsoonal
5 influenced Himalayan slopes is well simulated by the ANN model. However for the stations
6 in the central Asian deserts and at the southern Himalayan slopes, particularly for Jomsom,
7 which is located in the bottom of the deeply carved Kaligandaki valley in central Nepal, the
8 model clearly overestimates the precipitation amounts.

9

10 [Fig. 5]

11

12 For all other records the annual precipitation amounts are properly simulated with deviations
13 of annual precipitation sums below 20%. The seasonal variability of monthly precipitation
14 sums, with highest values during summer is well captured for the complete target area. The
15 locations of Darlag, Darwu and Tuotuohe (all situated at elevated sites on the Tibetan Plateau)
16 and Sikta (at the southern Himalayan slopes) receive a considerable amount of winter precipi-
17 tation, which is (although distinctly overestimated for the station Darlag) in general well cap-
18 tured by the ANN model. The interannual variability of precipitation rates is particularly ob-
19 vious for the monsoon season. The well documented 2009 drought over India and the Hima-
20 layas (Preethi et al., 2011) is clearly evident in the observed and modeled time series of pre-
21 cipitation sums for Jomsom, Phidim and Sikta. Likewise for the arid landscapes in the North-
22 ern part of the model domain, the major variations of annual precipitation amounts are well
23 captured. Particularly the obvious feature of low precipitation rates during 2009 and consider-
24 ably higher values in the following year are evident in observations and modeling results. The
25 interannual variability of moisture fluxes into the Western Tibetan Plateau and the accompa-
26 nying variability of precipitation rates is likewise well simulated by the modeling results. Par-
27 ticularly the extremely dry year 2009 at the station Shiquanhe is evident in both data sets. The
28 explained variance of the ANN model ranges from approximately 0.5 for the convective dom-
29 inated stations in the arid landscapes in the north of the study region to considerable 0.75 in
30 the monsoonal influenced areas south and east of the Tibetan Plateau.

31 Although, the validation was conducted exemplarily and more sophisticated and computational
32 demanding techniques (e.g. k-cross-fold-evaluation or an evaluation based on additional
33 data sets, which were neither used for the model calibration nor for the choice of an adequate

1 network architecture) would certainly better assess the overall performance of the model, the
2 results indicate, that both, the spatial and temporal variability are well captured by the statisti-
3 cal approach. Particularly the fact, that the local scale topographically induced precipitation
4 distribution coincides with with remote sensing derived precipitation products (Bookhagen
5 and Burbank, 2006; Shrestha et al., 2012) supports the feasibility of the suggested downscal-
6 ing approach.

7 Based on the gridded modeling results, a detailed analysis of the temporal and spatial precipi-
8 tation distribution in the target area and its essential influencing factors is given below.

9

10 [Fig. 6]

11 **4 Results**

12

13 **4.1 Spatial and temporal variability of precipitation rates**

14

15 The ANN model was utilized to estimate gridded monthly precipitation sums, the maximum
16 daily precipitation and the number of rainy days for each month with a horizontal resolution
17 of 1km² for the period from 1989 to 2011. The prominent features of the spatial, seasonal and
18 interannual variability of modeled precipitation rates were analyzed and are highlighted below
19 with emphasis on the winter and summer type circulation. Therefore the mean precipitation
20 sums for January and July are mapped in Fig. 7. To quantify the interannual variability the
21 coefficient of variation, defined as the ratio of the standard deviation by the mean precipita-
22 tion sum, was calculated cellwise. Further, for a rough estimation of the precipitation intensity
23 and frequency the percentage of the maximum daily precipitation of the monthly precipitation
24 sum is given in Fig. 7. Since the number of rainy days highly correlates with monthly precipi-
25 tation sums and the maximum daily intensity, we resign to map this additional predictant vari-
26 able.

27 As expected, the simulated large scale precipitation distribution in the target area is mainly
28 determined by the prevailing atmospheric modes. During winter season the circulation pattern
29 is characterized by the Asiatic high in the boundary layer and the southward shift of the 200
30 hPa jetstream. The target area is mainly dominated by dry conditions. Particularly for the
31 Tarim Basin no January precipitation was predicted for the entire period. Similarly the Low-
32 lands of India and the Red Basin show monthly precipitation sums below 20mm. The Tibetan

1 Plateau, especially the western part, which is located leeward of the Karakoram and Pamir
2 mountains, receives mean monthly precipitation sums below 30 mm and shows a large
3 interannual variability of precipitation rates ($cv > 2$). Meanwhile the Kunlun and Quilian
4 mountains act as a barrier to the prevailing westerly flow. The uplift of advected air masses
5 and the occasional passage of westerly disturbances result in considerable winter precipitation
6 amounts. For January the mean precipitation sums at the western slopes of the mountain rang-
7 es reach more than 50 mm, for the leeward slopes and the valley bottoms less than 20 mm are
8 characteristic. The rainfall occurs reliable and steadily, the interannual variability is small, the
9 low ratio of maximum daily precipitation and the monthly sum indicates a temporally uniform
10 precipitation distribution and the absence of extreme events (see Fig. 7). The maximum of
11 January precipitation occurs at the western margin of the Himalayas due to a stronger south-
12 ern branch of the 200 hPa jetstream. The windward slopes receive up to 150 mm in average
13 during January. The amounts of winter precipitation at the Himalayan slopes show a clear
14 gradient from west to east. As the Kunlun and Quilian Shan the Western Himalayas are char-
15 acterized by a comparably low variability of winter precipitation rates.

16

17 [Fig. 7]

18

19 During spring season the pressure gradients over Asia decrease. The enhanced radiative forc-
20 ing leads to occasional convective precipitation events, particularly over India and the south-
21 ern Himalayan Slopes, while the north of target area remains under dry conditions (figure not
22 shown). In July the summer type circulation pattern is fully established, the monsoonal flow
23 leads to intense moisture fluxes into the study region. Particularly the Indus-Ganges Low-
24 lands and the Himalayan slopes receive heavy rainfall with mean monthly sums of partially
25 more than 1000 mm at windward positions. Since the Indian lowlands are only rudimentarily
26 represented by our observations, the results of the approach for that particular subdomain
27 should be considered as less reliable. For the well represented Himalayan slopes the model
28 results indicate the occurrence of two high precipitation bands, as observed by Bookhagen
29 and Burbank (2006). The first discontinuous zone of high precipitation is located at the
30 windward sites of the first orographic barrier of the outer Himalayas at elevations between
31 1500 m and 2000 m. A second band of high precipitation occurs south of the highest Himala-
32 yan peaks at elevations between 2000 m and 2500 m. The zones of maximal precipitation are
33 followed by a sharp decrease above 4000 m. Particularly for the Southern Himalayan slopes,

1 the precipitation distribution during summer season results in a distinct differentiation of an-
2 nual precipitation sums (see Fig. 8b). The variability of monsoonal precipitation at the Hima-
3 layan slopes is low, particularly for the eastern Himalayas c_v -values below 0.1 were computed
4 by the ANN model. The leeward regions of the Trans-Himalayas receive less than 90 mm
5 average precipitation during July. Contemporaneously the Red Basin is under the influence of
6 the East-Asian monsoon and receives precipitation amounts of more than 300 mm in average
7 during July. For the windward slopes east of the Tibetan Plateau monthly precipitation sums
8 of up to 1000 mm were estimated. However the depiction of annual precipitation sums for the
9 Eastern margin of the Tibetan Plateau shows a scattered precipitation distribution, which
10 might indicate the appearance of statistical artefacts in that particular region. The interannual
11 variability of monsoonal precipitation in the Red Basin was found to be low with c_v -values
12 below 0.1. The precipitation distribution over the Tibetan Plateau shows a clear east-west
13 gradient during summer season. The east of the Plateau is penetrated by moist monsoonal air
14 masses due to the meridional orientation of the Three River Gorges. This results in monthly
15 precipitation sums of up to 150 mm. The western part is situated leeward of the Himalayan
16 and Karakoram mountain ranges and thus remains under dry conditions. For the valley bot-
17 toms the monthly precipitation estimates amount to less than 20 mm, for the elevated sites up
18 to 50 mm were computed. This indicates a rather convective precipitation regime by implica-
19 tion of the diurnal mountain-valley circulation. The interannual variability is remarkable
20 higher compared to advective dominated regions such as the windward slopes of the main
21 mountain ranges ($c_v > 0.4$, see Fig. 7). Likewise the higher ratio of maximum daily precipita-
22 tion and the monthly precipitation sum (partially 40 % of the monthly precipitation amount
23 fall within one day) indicates the occurrence sporadic precipitation events. The Quilian moun-
24 tains receive higher summer precipitation amounts of more than 70mm during July and mark
25 the border of the East-Asian monsoonal influence. The leeward slopes, the Tsaidam Depres-
26 sion in the south-east of the Quilian Shan, and the Tarim Basin are characterized by mean
27 monthly precipitation sums below 20 mm and a considerable larger interannual variability
28 with c_v -values ranging from 0.3 to 0.5. In the Tarim Basin the maximum of daily precipitation
29 exceeds 50% of the monthly precipitation sum. This indicates the importance of autochtho-
30 nous convective precipitation events for the northernmost part of the study region.

31 The estimated mean annual precipitation sums (Figure 8) reach 1500 to 2000 mm in the Low-
32 lands of India and up to more than 4000 mm at the southern slopes of the Central Himalayas.
33 The Himalayan valleys, located North of the first orographic barriers of the monsoonal cur-
34 rent, receive considerably reduced annual precipitation amounts in the order of 1200 to 1500

1 mm (Fig 8b). The Indian Lowlands and the eastern Himalayas receive more than 80% of the
2 annual rainfall during summer season. For the western Himalayas the percentage of summer
3 precipitation reaches barely 60 % of the annual amount. The annual precipitation estimates for
4 the Tibetan Plateau reveal a strong east-west gradient with amounts below 100 mm in the far
5 west and above 1000 mm in the monsoonal influenced eastern part. Particularly in Western
6 Tibet the valley bottoms are characterized by arid conditions with annual precipitation sums
7 below 100 mm, while the elevated sites reach values of up to 350 mm (Fig. 8c). The precipita-
8 tion estimates for the Kunlun mountains amount to approximately 400 to 600mm with maxi-
9 mum values in the far west due to an enhanced winter precipitation (DJF), which reaches up
10 to 50% of the annual precipitation sum. The annual precipitation over the Quilian Shan reach-
11 es 500 to 600 mm with highest values at the stronger monsoonal influenced east facing slopes.
12 The Tarim Basin is characterized by dry conditions throughout the year, the annual precipita-
13 tion sum amounts to less than 80mm. The convective precipitation during summer season
14 amounts to almost 90% of the annual sum.

15

16 [Fig. 8]

17

18 **4.2 Sensitivity analysis for large scale atmospheric and topographic predictor** 19 **variables**

20

21 In comparison to linear models, the complex structure of the ANN does not directly reveal
22 physically interpretable input-output relationships. Thus ANNs are often mentioned as Black-
23 Box-models (Schönwiese et al., 2010). For the identification of the particular synoptic and
24 local scale processes leading to a spatial and temporal precipitation variability in the target
25 area, a local sensitivity analysis was conducted and is exemplarily illustrated for four loca-
26 tions, which represent varying precipitation regimes in the study region (Fig. 9). Nearby loca-
27 tions in general show similar results of the sensitivity analysis. In each case one predictor var-
28 iable was chosen as a running variable – taking values between the 0.1 to 1.0 percentiles of
29 the learning sample, while all other predictors were set to constant values. For the assessment
30 of the model sensitivity to altering large scale atmospheric predictor variables (Fig. 9a) all
31 predictors (beside of the considered running variable) were set to their mean values (which is
32 0 for normalized values). The predicted precipitation amounts display the response of the
33 ANN model, i.e. the modeled precipitation amounts [mm/month], to modified values of the

1 considered predictor variables and provide an insight into the internal model structure. For the
2 assessment of the response of the ANN model to altering topographic characteristics of the
3 underlying surface, two sensitivity experiments under different large scale atmospheric condi-
4 tions were conducted. In order to investigate the model sensitivity to topographic characteris-
5 tics under dry conditions (Fig. 9b), the relative humidity at the 500hPa- and 200hPa-level was
6 set to 0 % and the scores of the first EOF were set to the minimum value, representing a typi-
7 cal winter type circulation pattern. All other predictor variables were set to their mean values.
8 For an assessment of the model sensitivity under moist conditions, the relative humidity was
9 set to 100% and the EOF1-scores were set to maximum, as characteristic for the summer cir-
10 culation type (Fig. 9c). Further a generalized sensitivity analysis for the maximum daily pre-
11 cipitation amounts was conducted for both, atmospheric and topographic precipitation
12 amounts (Fig. 9d). Therefore all predictors (beside of the running variable) were set to their
13 mean values.

14 The ANN signal of each predictor variable for the monthly precipitation sums and the maxi-
15 mum daily precipitation amount is plotted in Fig. 9. The station Sikta, situated near the South-
16 ern Nepali border, represents the monsoonal climate of the Indian Lowlands and the slopes of
17 the Himalayas. The first EOF (indicating the pressure gradient between the Asian continent
18 and the Indian Ocean) and the relative humidity (especially at 200 hPa) were found to be the
19 crucial large scale predictors for the observed precipitation rates. A strong positive pressure
20 gradient during summer season intensifies the monsoonal circulation and leads to enhanced
21 precipitation rates over the Indus-Ganges Lowlands and the Himalayan Arc. The positive re-
22 sponse to increasing values of second EOF scores (which are negatively correlated with the
23 SOI-Index) indicates a positive implication of El-Nino events for the monsoonal precipitation
24 amounts at first sight. However a further correlation analysis of the predictor variables reveals
25 a strong negative relationship ($r > 0.5$, $p = 0.95$) of the EOF2-scores and the 500 hPa relative
26 humidity during summer season for all stations located in the Indian Lowlands and at the
27 southern Himalayan slopes. For other regions of the target area, no significant correlation
28 could be identified. This indicates a decreased moisture flux into the target area during El-
29 Nino events, which is sufficiently captured by the assimilated ERA-Interim reanalysis. Partic-
30 ularly for the 2009 monsoon season the relative humidity fields of the reanalysis show a con-
31 siderable negative anomaly over India and the Himalayas (not shown). In combination with a
32 slight negative anomaly of the large scale pressure gradients, this results in reduced precipita-
33 tion rates predicted by the ANN model (see Fig. 6). The negative response to increasing val-
34 ues of the wind shear has to be interpreted with regard to the annual shift of the 200 hPa

1 jetstream. While the windshear over India during monsoon season is comparably low, the
2 winter circulation pattern is characterized by high wind speeds in the upper troposphere. Alt-
3 hough southward shift of the jetstream leads to the occasional passage of westerly disturb-
4 ances, the winter season is mainly dominated by dry synoptic conditions. For the local scale
5 precipitation distribution the wind effect parameter could be identified as the major topo-
6 graphic predictor variable for the Himalayan slopes, resulting in a considerable topographic
7 differentiation of the precipitation estimates. The model particularly shows a distinct response
8 to the wind-effect parameter under moist conditions, however even under dry atmospheric
9 circumstances, the estimates of monthly precipitation amounts show higher values at wind-
10 ward slopes (Fig. 9b & 9c). Such as the distribution of monthly precipitation sums, the sensi-
11 tivity analysis indicates that the topographic differentiation of maximum daily precipitation
12 rates for the Southern Himalayan slopes is primarily determined by the wind-effect parameter
13 (Fig. 9d). The negative response of increasing elevations implies the sharp precipitation de-
14 crease above 4000 m. The sensitivity analysis for Dawu (located on the eastern Tibetan Plat-
15 eau) shows a similar response for most of the synoptic and topographic predictor variables.
16 However, in comparison with the Southern Himalayan slopes, the precipitation estimates
17 show a clear positive response to increasing values of the relative elevation above the nearest
18 channel network under both, moist and dry large scale atmospheric conditions. Particularly
19 for the maximum daily precipitation amounts the response of the ANN model to variations of
20 Z_{rel} was found to be considerably larger than the influence of the wind effect. This indicates
21 the importance of convective precipitation events for the spatial precipitation distribution over
22 the eastern Tibetan Plateau and especially for the generation of intense precipitation events.
23 The fact, that the model distinctly responds to increasing values of the relative elevation, even
24 under dry atmospheric conditions, might indicate the importance of local water recycling for
25 the precipitation formation on the Tibetan Plateau as suggested e.g. by Kurita and Yamada,
26 (2008) and Yang et al., (2007). For the location of Xainza (Western Plateau) the ANN re-
27 sponse to variations of the wind effect seems to be negligible. Elevation and relative elevation
28 above the channel network were detected as the most influential predictors for the spatial pre-
29 cipitation distribution, indicating a rather convective precipitation regime over the Western
30 Tibetan Plateau. Again, the modeled monthly precipitation amounts increase with rising val-
31 ues of relative elevation under moist and dry large scale atmospheric conditions. The sensi-
32 tivity analysis for the location of Alar, located in the arid Tarim Basin, mainly reveals a cer-
33 tain response of the ANN model to variations of moisture fluxes into the Tarim basin, repre-
34 sented by the 500 hPa relative humidity of the ERA-Interim reanalysis. A slight positive re-

1 sponse to increased EOF1-scores is most likely due to isochronous development of the sum-
2 mer monsoon circulation pattern and the occurrence of convective precipitation events and
3 should not be interpreted as a monsoonal influence. Under dry atmospheric conditions, the
4 precipitation distribution over the homogenous Tarim Basin appears to be rather unaffected by
5 varying topographic settings. High values of relative humidity and the first EOF-scores lead
6 to distinct topographic differentiation of monthly precipitation rates, comparable with the
7 Western Tibetan Plateau, which is dominated by a convective precipitation regime. However,
8 it should be mentioned that such high values of relative humidity actually do not occur over
9 the Central Asian deserts.

10
11 [Fig. 9]

13 **5 Conclusions and Outlook**

14
15 The presented ANN based downscaling approach sufficiently captures the large and local
16 scale variations of the precipitation distribution in the highly structured target area. By means
17 of the integration of physically based terrain parameters, the approach addresses particular
18 local scale atmospheric processes and enables the statistical downscaling of fully distributed
19 precipitation fields in mountainous environments.

20 Especially for the monsoonal dominated precipitation regimes of the Indus-Ganges Lowlands,
21 the Himalayan slopes and the Red Basin the approach explains up to 70% of the variability of
22 monthly precipitation sums. However for the Kunlun and Quilian mountains, where precipita-
23 tion occurs mainly due to western circulation patterns, and for the convective dominated re-
24 gions, such as the Western Tibetan Plateau and the Tarim Basin, the results are less reliable
25 ($r^2=0.5$).

26 The trained ANN model stands out due to its non-linearity and its ability to capture the inter-
27 actions of related large scale atmospheric and topographic predictor variables and facilitates
28 the consideration of varying precipitation forming processes in different subregions of the
29 modeling domain. A subsequent local sensitivity analysis can reveal the influence of specific
30 predictor variables on the ANN output. While the large scale spatial variations and the sea-
31 sonal cycle of the monthly precipitation amounts were found to be determined by varying
32 circulation modes and moisture fluxes, as represented by the ERA-Interim reanalysis, the lo-

1 cal scale precipitation distribution was found to be highly influenced by topographic charac-
2 teristics. However the impact of the topographic parameters highly depends on the large scale
3 climatic regimes. Precisely for that reason complex Artificial neural networks are effective
4 modeling tools, particularly in comparison with linear models, which suggest a constant sta-
5 tistical relationship of predictor and predictant variables for the entire target area. While
6 windward and leeward positions were identified as the major topographic predictor for the
7 local scale spatial precipitation variations in the monsoonal dominated regions of India and
8 the Himalayas, the rather convective dominated precipitation regimes of the Western Tibetan
9 Plateau appear to be mainly influenced by the relative elevation above channel network and
10 the accompanied diurnal mountain-valley circulation.

11 The spatial resolution of the modeled precipitation rates of 1 km² is auspicious for climate
12 impact studies, e.g. for the analysis of climato-sensitive ecosystems and hydrological regimes.
13 However the focus of the presented study on monthly precipitation estimates still does not
14 satisfy the requirements of several geoscientific modeling approaches. Hence further research
15 needs to be done to generate spatial and temporal high resolution precipitation estimates.
16 Since the terrain induced precipitation-forming processes show a large temporal variability
17 due to varying mesoscale atmospheric characteristics, the assessment of daily precipitation
18 rates remains challenging. Böhner (1996) illustrates, that the representation of precipitation
19 amounts for monthly observations in Central Asia remains below 200 km. This is particularly
20 valid for the convective dominated regions of the target area and indicates the heterogeneity
21 of precipitation observations in complex terrain. The daily precipitation amounts in the study
22 region are determined by mesoscale atmospheric processes, such as the passage of tropical
23 and westerly disturbances or the development of convective clusters, which are not sufficient-
24 ly represented by limited resolution climate models or reanalysis products. The mesoscale
25 atmospheric patterns however are crucial for the identification of the flow direction and the
26 moisture fluxes on a daily time scale. This further increases atmospheric heterogeneity in
27 mountainous regions and impedes the statistical analysis of interactions between the atmos-
28 pheric circulation and the underlying topographic characteristics. State of the art dynamical
29 downscaling models can be effective alternatives for the simulation of mesoscale atmospheric
30 processes, but due to their high computational demands and their requirements for high quali-
31 ty input data, most studies focus on a limited spatial domain or time frame. So far the WRF-
32 based High Asia Refined analysis (Maussion et al., 2014) is the only data set known to the
33 authors, which adequately captures the mesoscale climatic variability for the entire target re-
34 gion of this study for the reasonable period from 2001 to 2011. Although the resolution of 10

1 km still does not satisfy the needs of many climate impact investigations, the data set could
2 provide improved free atmospheric predictor variables for statistical downscaling applica-
3 tions. The combination of dynamical downscaling and a the presented statistical approach
4 appears to be auspicious for the analysis of mesoscale atmospheric conditions and its modifi-
5 cation due to local scale topographic characteristics and should be considered for further re-
6 search.

7

8 **Acknowledgements**

9

10 The ERA-Interim reanalysis fields were freely provided by the ECMWF. We appreciate the
11 supply of daily meteorological observations by the Department of Hydrology and
12 Meteorology (Kathmandu, Nepal) and the Chinese Meteorological Administration (Beijing,
13 China). The study was funded by the Federal Ministry of Education and Research (Berlin,
14 Germany) in the context of the Project CLASH (Climate variability and landscape dynamics
15 in Southeast-Tibet and the eastern Himalaya during the late Holocene reconstructed from tree
16 rings, soils and climate modeling).

17

18

19 **References**

20

21 Akhtar, M., Ahmad, N. and Booij, M. J.: The impact of climate change on the water resources
22 of Hindukush–Karakorum–Himalaya region under different glacier coverage scenarios,
23 *Journal of Hydrology*, 355(1–4), 148–163, doi:10.1016/j.jhydrol.2008.03.015, 2008.

24 Bao, X. and Zhang, F.: Evaluation of NCEP/CFSR, NCEP/NCAR, ERA-Interim and ERA-40
25 Reanalysis Datasets against Independent Sounding Observations over the Tibetan Plateau,
26 *Journal of Climate*, 120630072710003, doi:10.1175/JCLI-D-12-00056.1, 2012.

27 Barros, A. P., Joshi, M., Putkonen, J. and Burbank, D. W.: A study of the 1999 monsoon
28 rainfall in a mountainous region in central Nepal using TRMM products and rain gauge
29 observations, *Geophys. Res. Lett.*, 27(22), 3683–3686, doi:10.1029/2000GL011827, 2000.

30 Barry, R. G.: Recent advances in mountain climate research, *Theor Appl Climatol*, 110(4),
31 549–553, doi:10.1007/s00704-012-0695-x, 2012.

32 Basheer, I. A. and Hajmeer, M.: Artificial neural networks: fundamentals, computing, design,
33 and application, *J. Microbiol. Methods*, 43(1), 3–31, 2000.

34 Berrisford, P., Dee, D., Fielding, K., Fuentes, M., Kallberg, P., Kobayashi, S. and Uppala, S.:
35 The ERA-Interim Archive, ERA report series [online] Available from:

- 1 <http://www.ecmwf.int/publications/library/do/references/list/782009> (Accessed 15 January
2 2013), 2009.
- 3 Böhner, J.: Säkulare Klimaschwankungen und rezente Klimatrends Zentral- und Hochasiens,
4 Goltze., 1996.
- 5 Böhner, J.: General climatic controls and topoclimatic variations in Central and High Asia,
6 *Boreas*, 35(2), 279–295, doi:10.1080/03009480500456073, 2006.
- 7 Böhner, J. and AntoniĆ, O.: Chapter 8 Land-Surface Parameters Specific to Topo-Climatology,
8 in *Developments in Soil Science*, vol. Volume 33, edited by Tomislav Hengl and Hannes I.
9 Reuter, pp. 195–226, Elsevier. [online] Available from:
10 <http://www.sciencedirect.com/science/article/pii/S0166248108000081> (Accessed 15 January
11 2013), 2009.
- 12 Bookhagen, B. and Burbank, D. W.: Topography, relief, and TRMM-derived rainfall
13 variations along the Himalaya, *Geophys. Res. Lett.*, 33(8), L08405,
14 doi:10.1029/2006GL026037, 2006.
- 15 Buishand, T. A.: Some methods for testing the homogeneity of rainfall records, *Journal of*
16 *Hydrology*, 58(1), 11–27, 1982.
- 17 Chattopadhyay, S.: Feed forward Artificial Neural Network model to predict the average
18 summer-monsoon rainfall in India, *Acta Geophys.*, 55(3), 369–382, doi:10.2478/s11600-007-
19 0020-8, 2007.
- 20 Chen, F., Liu, Y., Liu, Q. and Li, X.: Spatial downscaling of TRMM 3B43 precipitation
21 considering spatial heterogeneity, *International Journal of Remote Sensing*, 35(9), 3074–3093,
22 doi:10.1080/01431161.2014.902550, 2014.
- 23 Corbosiero, K. L. and Molinari, J.: The Effects of Vertical Wind Shear on the Distribution of
24 Convection in Tropical Cyclones, *Mon. Wea. Rev.*, 130(8), 2110–2123, doi:10.1175/1520-
25 0493(2002)130<2110:TEOVWS>2.0.CO;2, 2002.
- 26 Coulibaly, P., Dibikey, Y. B. and Anctil, F.: Downscaling Precipitation and Temperature with
27 Temporal Neural Networks, *J. Hydrometeorol.*, 6(4), 483–496, doi:10.1175/JHM409.1, 2005.
- 28 Daly, C., Neilson, R. P. and Phillips, D. L.: A Statistical-Topographic Model for Mapping
29 Climatological Precipitation over Mountainous Terrain, *J. Appl. Meteor.*, 33(2), 140–158,
30 doi:10.1175/1520-0450(1994)033<0140:ASTMFM>2.0.CO;2, 1994.
- 31 Dawson, C. W. and Wilby, R. L.: Hydrological modelling using artificial neural networks,
32 *Progress in Physical Geography*, 25(1), 80–108, doi:10.1177/030913330102500104, 2001.
- 33 Dee, D. P., Uppala, S. M., Simmons, A. J., Berrisford, P., Poli, P., Kobayashi, S., Andrae, U.,
34 Balmaseda, M. A., Balsamo, G. and Bauer, P.: The ERA-Interim reanalysis: Configuration
35 and performance of the data assimilation system, *Quarterly Journal of the Royal*
36 *Meteorological Society*, 137(656), 553–597, 2011.
- 37 Dibikey, Y. B. and Coulibaly, P.: Temporal neural networks for downscaling climate variability
38 and extremes, *Neural Networks*, 19(2), 135–144, doi:10.1016/j.neunet.2006.01.003, 2006.

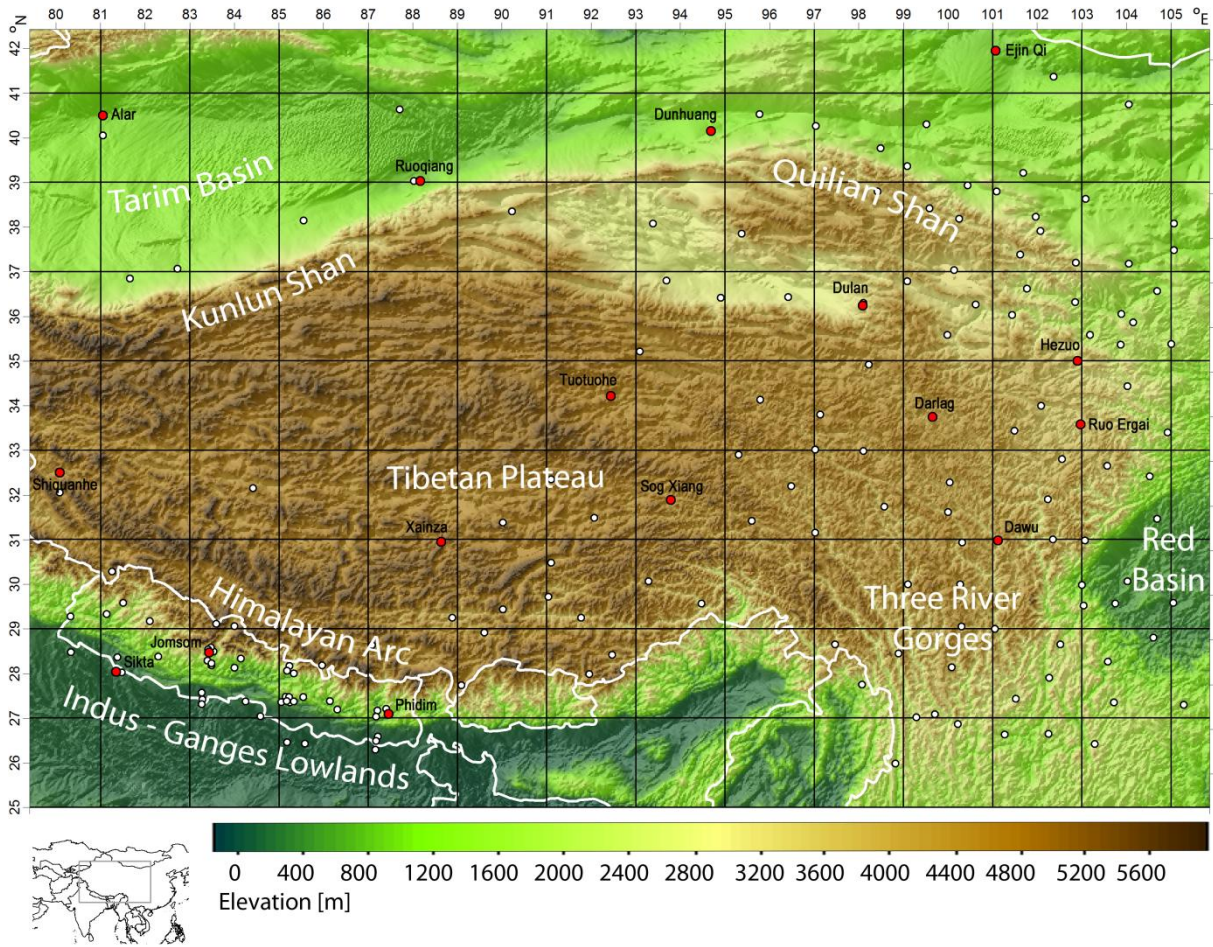
- 1 Dimri, A. P., Yasunari, T., Wiltshire, A., Kumar, P., Mathison, C., Ridley, J. and Jacob, D.:
2 Application of regional climate models to the Indian winter monsoon over the western
3 Himalayas, *Sci. Total Environ.*, 468-469 Suppl, S36–47, doi:10.1016/j.scitotenv.2013.01.040,
4 2013.
- 5 Domrös, M.: *The Climate of China*, Springer., 1988.
- 6 Farr, T. G., Rosen, P. A., Caro, E., Crippen, R., Duren, R., Hensley, S., Kobrick, M., Paller,
7 M., Rodriguez, E. and Roth, L.: The shuttle radar topography mission, *Reviews of*
8 *Geophysics*, 45(2), RG2004, 2007.
- 9 Filippi, L., Palazzi, E., Von Hardenberg, J. and Provenzale, A.: Multidecadal Variations in the
10 Relationship between the NAO and Winter Precipitation in the Hindu Kush–Karakoram, *J.*
11 *Climate*, 27(20), 7890–7902, doi:10.1175/JCLI-D-14-00286.1, 2014.
- 12 Frank, W. M. and Ritchie, E. A.: Effects of Vertical Wind Shear on the Intensity and Structure
13 of Numerically Simulated Hurricanes, *Mon. Wea. Rev.*, 129(9), 2249–2269,
14 doi:10.1175/1520-0493(2001)129<2249:EOVWSO>2.0.CO;2, 2001.
- 15 Gao, L., Bernhardt, M. and Schulz, K.: Elevation correction of ERA-Interim temperature data
16 in complex terrain, *Hydrol. Earth Syst. Sci.*, 16(12), 4661–4673, doi:10.5194/hess-16-4661-
17 2012, 2012.
- 18 Gerlitz, L.: Using fuzzyfied regression trees for statistical downscaling and regionalization of
19 near surface temperatures in complex terrain,, 2014.
- 20 Gerlitz, L., Conrad, O., Thomas, A. and Bhner, J.: Warming patterns over the Tibetan Plateau
21 and adjacent lowlands derived from elevation- and bias -corrected ERA-Interim data, *Clim*
22 *Res*, 58(3), 235–246, doi:10.3354/cr01193, 2014.
- 23 Guan, H., Hsu, H.-H., Makhnin, O., Xie, H. and Wilson, J. L.: Examination of selected
24 atmospheric and orographic effects on monthly precipitation of Taiwan using the ASOAdEK
25 model, *Int. J. Climatol.*, 29(8), 1171–1181, doi:10.1002/joc.1762, 2009.
- 26 Günther, F. and Fritsch, S.: neuralnet: Training of neural networks, *The R journal*, 2(1), 30–
27 38, 2010.
- 28 Hannachi, A., Jolliffe, I. T. and Stephenson, D. B.: Empirical orthogonal functions and related
29 techniques in atmospheric science: A review, *Int. J. Climatol.*, 27(9), 1119–1152,
30 doi:10.1002/joc.1499, 2007.
- 31 Hannachi, A., Jolliffe, I. T., Stephenson, D. B. and Trendafilov, N.: In search of simple
32 structures in climate: simplifying EOFs, *Int. J. Climatol.*, 26(1), 7–28, doi:10.1002/joc.1243,
33 2006.
- 34 Hecht-Nielsen, R.: Theory of the backpropagation neural network, in , *International Joint*
35 *Conference on Neural Networks*, 1989. IJCNN, pp. 593–605 vol.1., 1989.
- 36 Hovermann, J. and Wenying, W.: *Reports on the Northeastern Part of the Qighai-Xizang*
37 *Plateau*, Lubrecht & Cramer Ltd., 1987.

- 1 Immerzeel, W. W. and Bierkens, M. F. P.: Seasonal prediction of monsoon rainfall in three
2 Asian river basins: the importance of snow cover on the Tibetan Plateau, *Int. J. Climatol.*,
3 30(12), 1835–1842, doi:10.1002/joc.2033, 2010.
- 4 Jain, A. and Kumar, A. M.: Hybrid neural network models for hydrologic time series
5 forecasting, *Applied Soft Computing*, 7(2), 585–592, doi:10.1016/j.asoc.2006.03.002, 2007.
- 6 Jin-Huan, Z. H. U., Shu-Po, M. A., Han, Z. O. U., Li-Bo, Z. and Peng, L. I.: Evaluation of
7 reanalysis products with in situ GPS sounding observations in the Eastern Himalayas,
8 *Atmospheric and Oceanic Science Letters*, 7(1), 17–22, 2013.
- 9 Kirono, D. G. C., Tapper, N. J. and McBride, J. L.: Documenting Indonesian Rainfall in the
10 1997/1998 El Niño Event, *Physical Geography*, 20(5), 422–435,
11 doi:10.1080/02723646.1999.10642687, 1999.
- 12 Kumar, null, Rajagopalan, null and Cane, null: On the weakening relationship between the
13 indian monsoon and ENSO, *Science*, 284(5423), 2156–2159, 1999.
- 14 Kurita, N. and Yamada, H.: The Role of Local Moisture Recycling Evaluated Using Stable
15 Isotope Data from over the Middle of the Tibetan Plateau during the Monsoon Season, *J.*
16 *Hydrometeor*, 9(4), 760–775, doi:10.1175/2007JHM945.1, 2008.
- 17 Li, C. and Yanai, M.: The Onset and Interannual Variability of the Asian Summer Monsoon in
18 Relation to Land–Sea Thermal Contrast, *J. Climate*, 9(2), 358–375, doi:10.1175/1520-
19 0442(1996)009<0358:TOAIVO>2.0.CO;2, 1996.
- 20 Mall, R. K., Singh, R., Gupta, A., Srinivasan, G. and Rathore, L. S.: Impact of Climate
21 Change on Indian Agriculture: A Review, *Climatic Change*, 78(2-4), 445–478,
22 doi:10.1007/s10584-005-9042-x, 2006.
- 23 Maraun, D., Wetterhall, F., Ireson, A. M., Chandler, R. E., Kendon, E. J., Widmann, M.,
24 Brienen, S., Rust, H. W., Sauter, T., Theme\s sl, M. and others: Precipitation downscaling
25 under climate change: recent developments to bridge the gap between dynamical models and
26 the end user, *Reviews of Geophysics*, 48(3) [online] Available from:
27 <http://onlinelibrary.wiley.com/doi/10.1029/2009RG000314/full> (Accessed 28 October 2014),
28 2010.
- 29 Matthews, R. B., Kropff, M. J., Horie, T. and Bachelet, D.: Simulating the impact of climate
30 change on rice production in Asia and evaluating options for adaptation, *Agricultural Systems*,
31 54(3), 399–425, doi:10.1016/S0308-521X(95)00060-I, 1997.
- 32 Maussion, F., Scherer, D., Mölg, T., Collier, E., Curio, J. and Finkelburg, R.: Precipitation
33 Seasonality and Variability over the Tibetan Plateau as Resolved by the High Asia
34 Reanalysis*, *J. Climate*, 27(5), 1910–1927, doi:10.1175/JCLI-D-13-00282.1, 2014.
- 35 Mekanik, F., Imteaz, M. A., Gato-Trinidad, S. and Elmahdi, A.: Multiple regression and
36 Artificial Neural Network for long-term rainfall forecasting using large scale climate modes,
37 *Journal of Hydrology*, 503, 11–21, doi:10.1016/j.jhydrol.2013.08.035, 2013.
- 38 Özesmi, S. L. and Özesmi, U.: An artificial neural network approach to spatial habitat
39 modelling with interspecific interaction, *Ecological Modelling*, 116(1), 15–31,
40 doi:10.1016/S0304-3800(98)00149-5, 1999.

- 1 Parth Sarthi, P., Agrawal, A. and Rana, A.: Possible future changes in cyclonic storms in the
2 Bay of Bengal, India under warmer climate, *Int. J. Climatol.*, n/a–n/a, doi:10.1002/joc.4053,
3 2014.
- 4 Peings, Y. and Douville, H.: Influence of the Eurasian snow cover on the Indian summer
5 monsoon variability in observed climatologies and CMIP3 simulations, *Clim Dyn*, 34(5),
6 643–660, doi:10.1007/s00382-009-0565-0, 2010.
- 7 Pokhrel, S., Chaudhari, H. S., Saha, S. K., Dhakate, A., Yadav, R. K., Salunke, K., Mahapatra,
8 S. and Rao, S. A.: ENSO, IOD and Indian Summer Monsoon in NCEP climate forecast
9 system, *Clim Dyn*, 39(9-10), 2143–2165, doi:10.1007/s00382-012-1349-5, 2012.
- 10 Preethi, B., Revadekar, J. V. and Kripalani, R. H.: Anomalous behaviour of the Indian summer
11 monsoon 2009, *J Earth Syst Sci*, 120(5), 783–794, doi:10.1007/s12040-011-0112-3, 2011.
- 12 Prodhomme, C., Terray, P., Masson, S., Boschhat, G. and Izumo, T.: Oceanic factors
13 controlling the Indian summer monsoon onset in a coupled model, *Clim Dyn*, 1–26,
14 doi:10.1007/s00382-014-2200-y, 2014.
- 15 RanjanNayak, D., Mahapatra, A. and Mishra, P.: A Survey on Rainfall Prediction using
16 Artificial Neural Network, *International Journal of Computer Applications*, 72(16), 32–40,
17 doi:10.5120/12580-9217, 2013.
- 18 Romatschke, U., Medina, S. and Houze, R. A.: Regional, Seasonal, and Diurnal Variations of
19 Extreme Convection in the South Asian Region, *J. Climate*, 23(2), 419–439,
20 doi:10.1175/2009JCLI3140.1, 2010.
- 21 Sankar, S., Kumar, M. R. R. and Reason, C.: On the relative roles of El Nino and Indian
22 Ocean Dipole events on the Monsoon Onset over Kerala, *Theor Appl Climatol*, 103(3-4),
23 359–374, doi:10.1007/s00704-010-0306-7, 2011.
- 24 Sauter, T., Schneider, C., Kilian, R. and Moritz, M.: Simulation and analysis of runoff from a
25 partly glaciated meso-scale catchment area in Patagonia using an artificial neural network,
26 *Hydrol. Process.*, 23(7), 1019–1030, doi:10.1002/hyp.7210, 2009.
- 27 Sauter, T. and Venema, V.: Natural Three-Dimensional Predictor Domains for Statistical
28 Precipitation Downscaling, *J. Climate*, 24(23), 6132–6145, doi:10.1175/2011JCLI4155.1,
29 2011.
- 30 Schönwiese, C.-D., Walter, A. and Brinckmann, S.: Statistical assessments of anthropogenic
31 and natural global climate forcing. An update, *Meteorologische Zeitschrift*, 19(1), 3–10,
32 doi:10.1127/0941-2948/2010/0421, 2010.
- 33 Schoof, J. T.: Statistical Downscaling in Climatology, *Geography Compass*, 7(4), 249–265,
34 doi:10.1111/gec3.12036, 2013.
- 35 Schoof, J. t. and Pryor, S. c.: Downscaling temperature and precipitation: a comparison of
36 regression-based methods and artificial neural networks, *Int. J. Climatol.*, 21(7), 773–790,
37 doi:10.1002/joc.655, 2001.

- 1 Shrestha, D., Singh, P. and Nakamura, K.: Spatiotemporal variation of rainfall over the central
2 Himalayan region revealed by TRMM Precipitation Radar, *J. Geophys. Res.*, 117(D22),
3 D22106, doi:10.1029/2012JD018140, 2012.
- 4 Shrestha, M. L.: Interannual variation of summer monsoon rainfall over Nepal and its relation
5 to Southern Oscillation Index, *Meteorol Atmos Phys*, 75(1-2), 21–28,
6 doi:10.1007/s007030070012, 2000.
- 7 Shukla, R. P., Tripathi, K. C., Pandey, A. C. and Das, I. M. L.: Prediction of Indian summer
8 monsoon rainfall using Niño indices: A neural network approach, *Atmospheric Research*,
9 102(1–2), 99–109, doi:10.1016/j.atmosres.2011.06.013, 2011.
- 10 Sigdel, M. and Ikeda, M.: Summer Monsoon Rainfall over Nepal Related with Large-Scale
11 Atmospheric Circulations, *Journal of Earth Science & Climatic Change*, 03(02),
12 doi:10.4172/2157-7617.1000112, 2012.
- 13 Singh, P. and Borah, B.: Indian summer monsoon rainfall prediction using artificial neural
14 network, *Stoch Environ Res Risk Assess*, 27(7), 1585–1599, doi:10.1007/s00477-013-0695-0,
15 2013.
- 16 Slingo, J. M. and Annamalai, H.: 1997: The El Niño of the Century and the Response of the
17 Indian Summer Monsoon, *Mon. Wea. Rev.*, 128(6), 1778–1797, doi:10.1175/1520-
18 0493(2000)128<1778:TENOOT>2.0.CO;2, 2000.
- 19 Suprit, K. and Shankar, D.: Resolving orographic rainfall on the Indian west coast, *Int. J.*
20 *Climatol.*, 28(5), 643–657, doi:10.1002/joc.1566, 2008.
- 21 Tomassetti, B., Verdecchia, M. and Giorgi, F.: NN5: A neural network based approach for the
22 downscaling of precipitation fields – Model description and preliminary results, *Journal of*
23 *Hydrology*, 367(1–2), 14–26, doi:10.1016/j.jhydrol.2008.12.017, 2009.
- 24 Wang, A. and Zeng, X.: Evaluation of multireanalysis products with in situ observations over
25 the Tibetan Plateau, *Journal of Geophysical Research*, 117(D5), D05102, 2012.
- 26 Wang, D., Xie, Q., Du, Y., Wang, W. and Chen, J.: The 1997–1998 warm event in the South
27 China Sea, *Chin. Sci. Bull.*, 47(14), 1221–1227, doi:10.1007/BF02907614, 2002.
- 28 Wang, H. and He, S.: Weakening relationship between East Asian winter monsoon and ENSO
29 after mid-1970s, *Chin. Sci. Bull.*, 57(27), 3535–3540, doi:10.1007/s11434-012-5285-x, 2012.
- 30 Wingo, M. T. and Cecil, D. J.: Effects of Vertical Wind Shear on Tropical Cyclone
31 Precipitation, *Mon. Wea. Rev.*, 138(3), 645–662, doi:10.1175/2009MWR2921.1, 2009.
- 32 Wulf, H., Bookhagen, B. and Scherler, D.: Seasonal precipitation gradients and their impact
33 on fluvial sediment flux in the Northwest Himalaya, *Geomorphology*, 118(1–2), 13–21,
34 doi:10.1016/j.geomorph.2009.12.003, 2010.
- 35 Xu, Z. X., Chen, Y. N. and Li, J. Y.: Impact of climate change on water resources in the Tarim
36 River basin, *Water Resources Management*, 18(5), 439–458, 2004.
- 37 Yang, M., Yao, T., Gou, X. and Tang, H.: Water Recycling between the Land Surface and
38 Atmosphere on the Northern Tibetan Plateau: A Case Study at Flat Observation Sites, Arctic,
39 Antarctic, and Alpine Research, 39(4), 694–698, 2007.

1



2

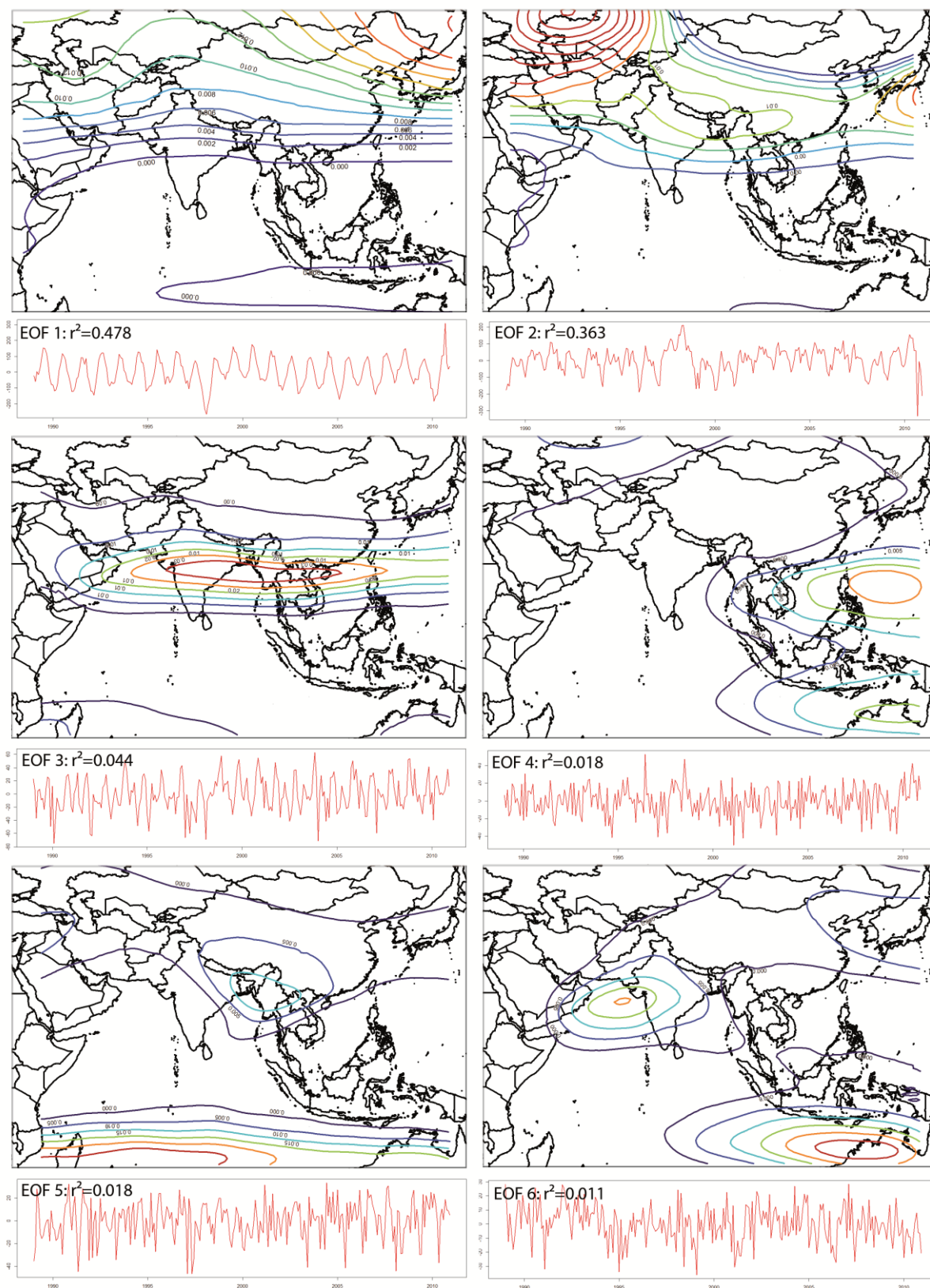
3

4

5

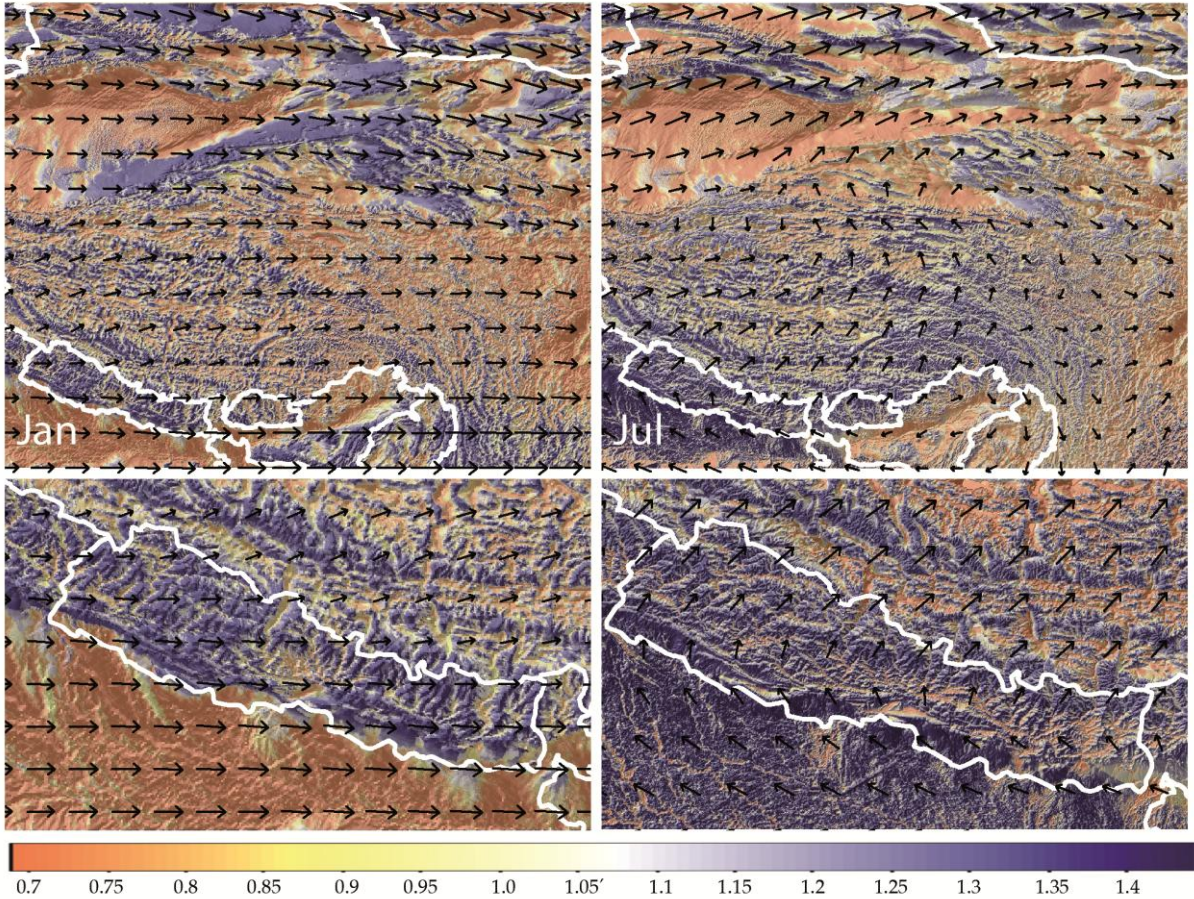
6

Fig 1: The target area and its main geomorphological features. The white dots indicate the locations of meteorological stations used for the implementation of the statistical downscaling model. The locations marked in red were used for the model evaluation.

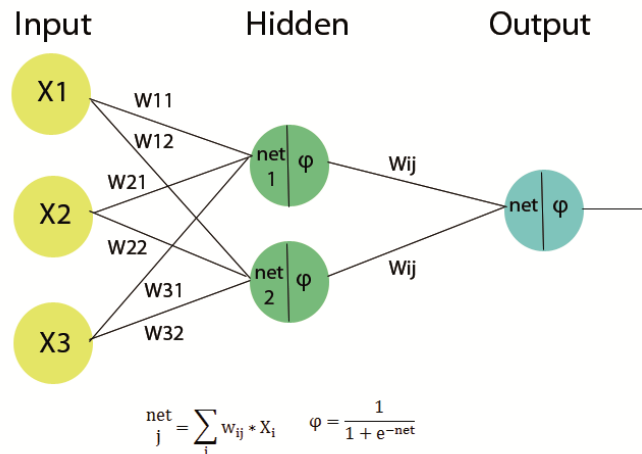


1
2
3
4
5

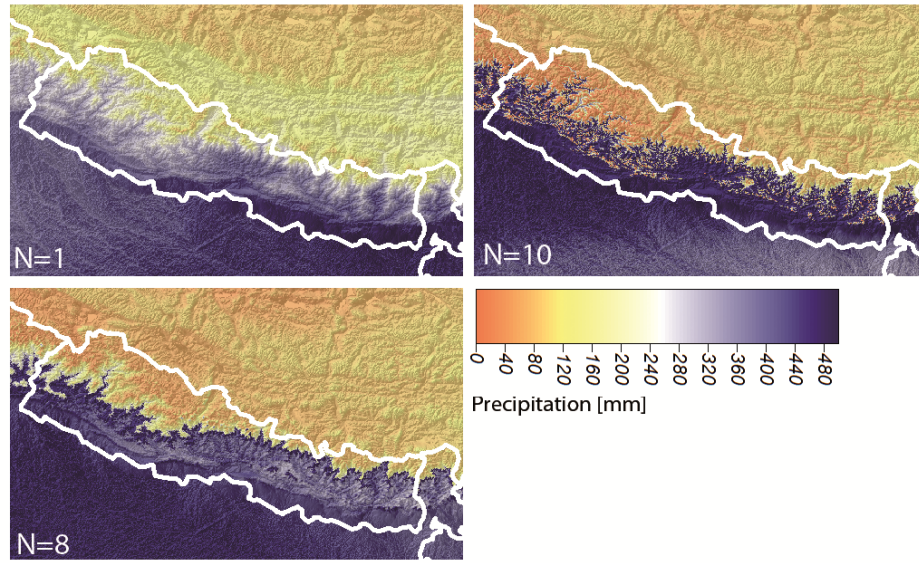
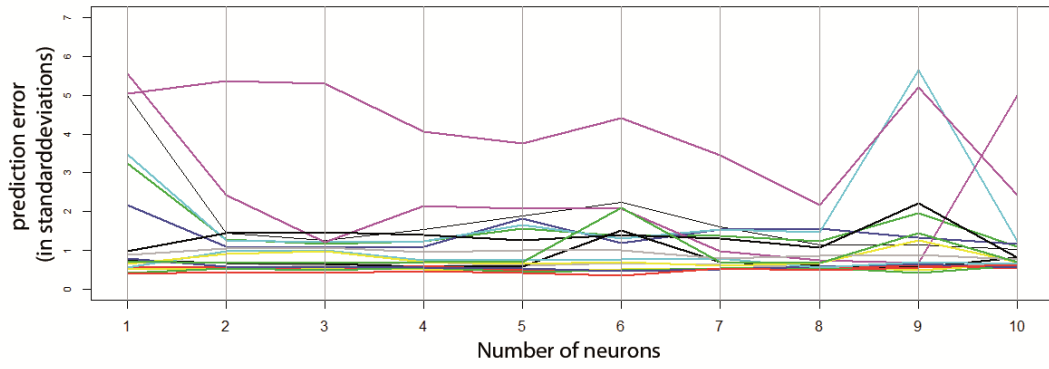
Fig. 2: Spatial modes and time series of scores for the first 6 EOFs of the 500 hPa GPH anomaly over the macrogeographical region. Blue lines indicate low, red lines high values of the particular EOF.



1
2
3
4
Fig. 3 The spatial distribution of the wind effect parameter for January and July 2010. The arrows represent the 500 hPa ERA-Interim wind field



5
6
7
8
9
Fig. 4 : Schematic structure of a feed-forward artificial neural network model and the equations for the integration function net_j and the activation function φ



1
2
3
4
5

Fig. 5: Normalized prediction error of various ANN architectures for 18 independent observational records (top) and the modeled distribution of precipitation sums for July 2010 over Nepal based on ANN architectures with N=1, N=8 and N=10 neurons.

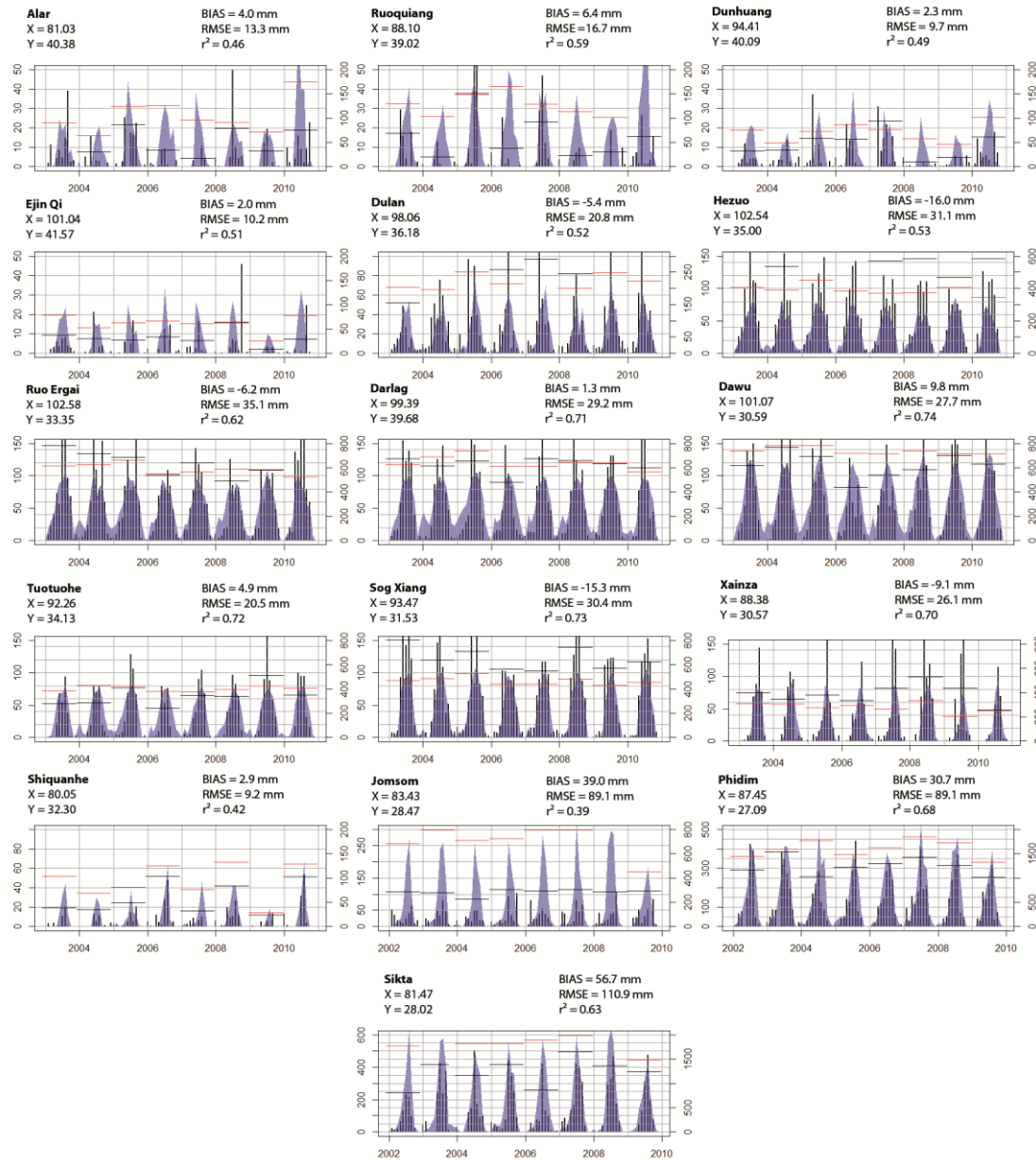
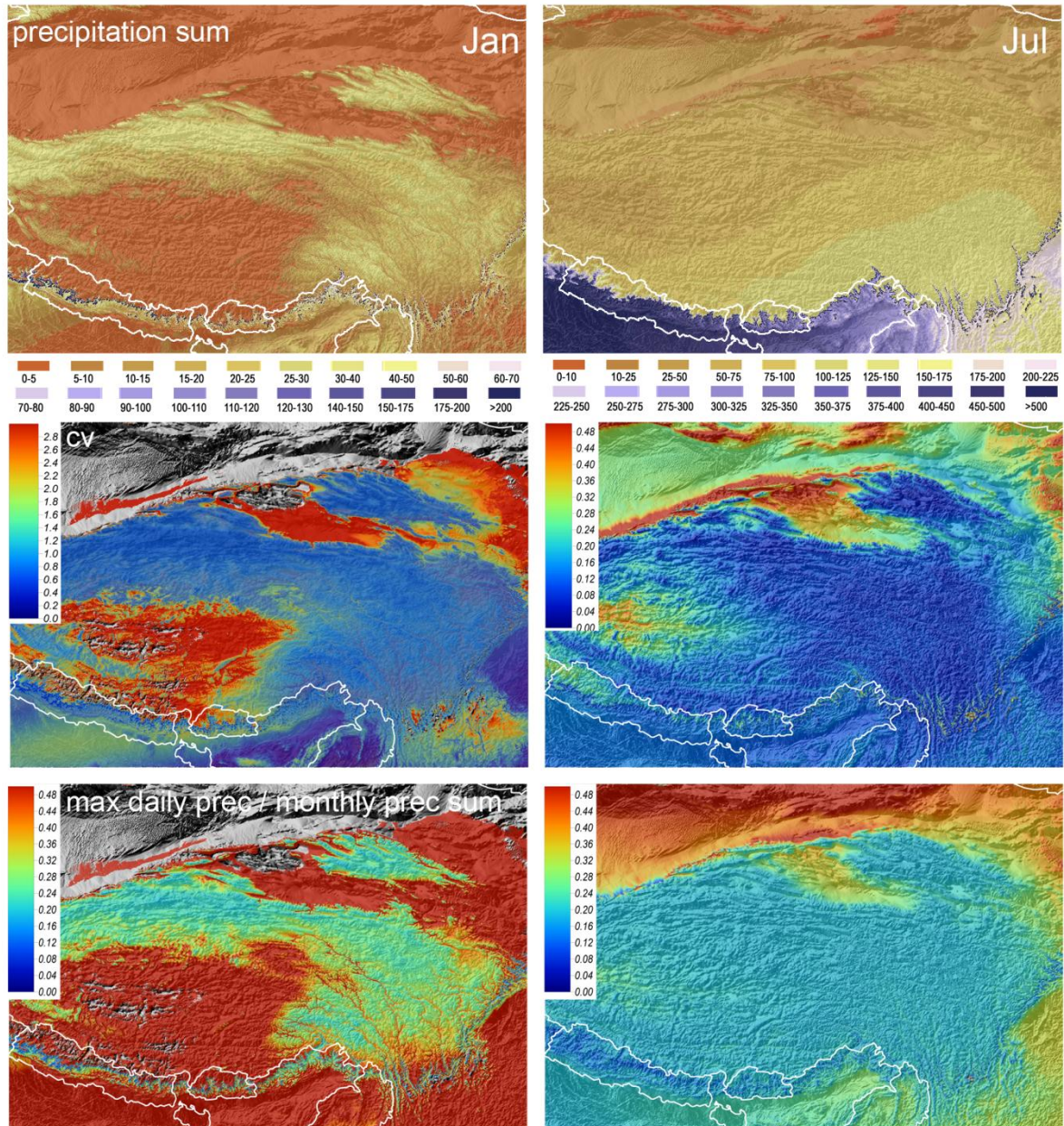


Fig. 6: Observed (black bars) and modeled (polygons) monthly precipitation sums [mm/month] (left Y-axis) and observed (black lines) and modeled (red lines) annual precipitation sums [mm/a] (right Y-axis) for 16 stations of the evaluation data set. The scale of the Y-axis is adapted to the maximum precipitation amount at each station respectively.

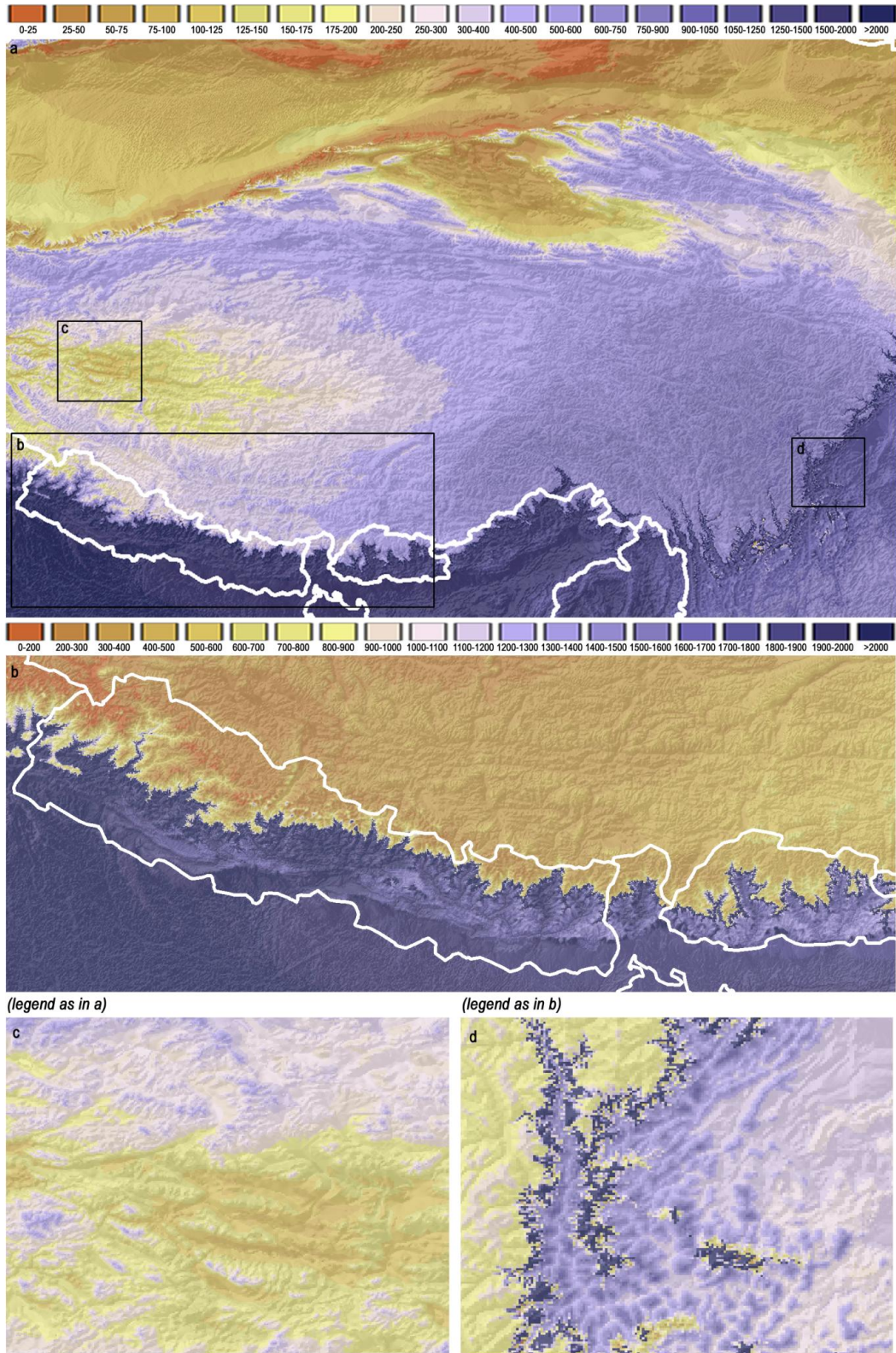
1
2
3
4
5
6
7



1

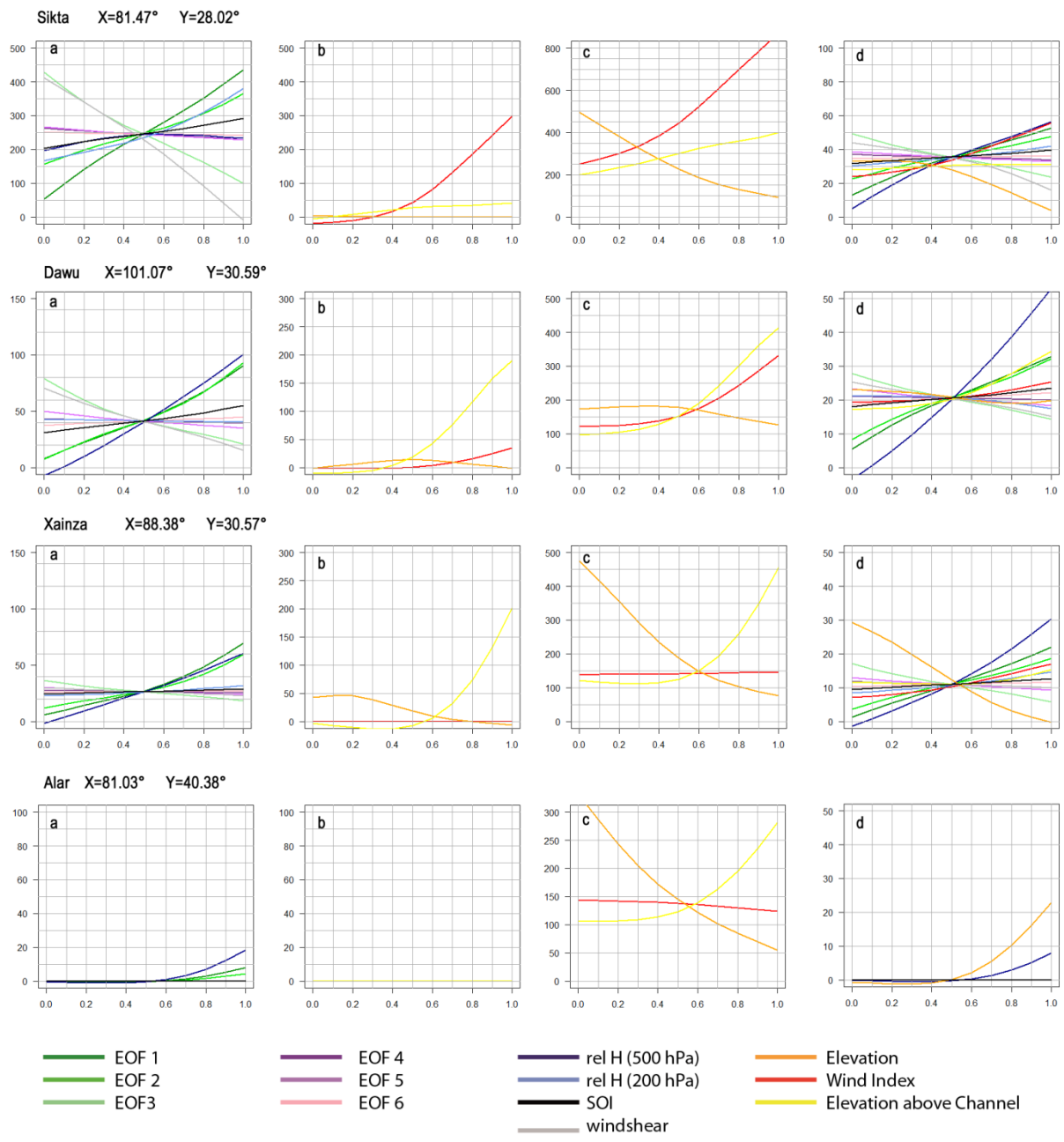
2
3

Fig. 7: Mean monthly precipitation sum [mm] (top), coefficient of variation (middle) and the ratio of maximum daily precipitation and the monthly sum (bottom) for January (left) and July (right).



1
2
3
4

Fig. 8: Modeled mean annual precipitation sums [mm] for the entire target domain (a) and enlargements of the Central Himalayan Arc (b), the Western Tibetan Plateau (c) and the margins of the Red Basin (d).



1
2
3
4
5
6
7
8
9

Fig. 9: Sensitivity analysis of the ANN model for the atmospheric and topographic predictor variables at selected locations. Values are in [mm].

(a) Sensitivity of the modeled monthly precipitation sums to altering values of large scal atmospheric predictor variables. (b) Sensitivity of monthly precipitation sums to topographic predictor variables under dry conditions. (c) Sensitivity of monthly precipitation sums to topographic predictor variables under moist conditions. (d) Generalized sensitivity analysis of maximum daily precipitation amounts.